České vysoké učení technické v Praze
Fakulta jaderná a fyzikálně inženýrská

Katedra fyziky
Jaderná a částicová fyzika

Měření multiplicity ve srážkách těžkých iontů v rámci experimentu ALICE v průběhu LHC Run 3

VÝZKUMNÝ ÚKOL

Vypracovala: Helena Hesounová
Vedoucí práce: prof. Jesús Guillermo Contreras Nuño, Ph.D.
Rok: 2023

Czech Technical University in Prague
Faculty of Nuclear Sciences and Physical Engineering

Department of Physics
Nuclear and Particle Physics

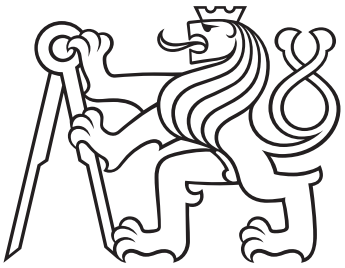

Measurement of multiplicity in heavy-ion collisions with ALICE during the LHC Run 3

RESEARCH TASK

Author: Helena Hesounová
Supervisor: prof. Jesús Guillermo Contreras Nuño, Ph.D.
Year: 2023

FAKULTA JADERNÁ A FYZIKÁLNĚ INŽENÝRSKÁ
KATEDRA FYZIKY

VÝZKUMNÝ ÚKOL

Akademický rok: 2022/2023

Student: Bc. Helena Hesounová

Studijní program: Jaderná a částicová fyzika

Vedoucí úkolu: prof. Jesus Guillermo Contreras Nuño, Ph.D.,
Katedra fyziky, Fakulta jaderná a fyzikálně inženýrská ČVUT v Praze

Název úkolu
(česky):
Měření multiplicity ve srážkách těžkých iontů v rámci experimentu ALICE v průběhu Run 3

(anglicky):
Mesurement of multiplicity in heavy-ion collisions with ALICE during the LHC Run 3

Jazyk VÚ: Angličtina

Pokyny pro vypracování:
1) Vypracování rešerše na téma:
a) Měření multiplicity ve srážkách těžkých iontů na experimentu ALICE
b) Modely multiplicity ve srážkách těžkých iontů
2) Analýza multiplicity ze srážek těžkých iontů naměřené pomocí detektoru ALICE

Literatura:
[1] ALICE Collaboration: Centrality dependence of the charged-particle multiplicity density at midrapidity in Pb-Pb collisions at sqrt(s_NN) = 5.02 TeV, Phys.Rev.Lett. 116 (2016) 22, 222302
[2] ALICE Collaboration: Centrality and pseudorapidity dependence of the charged-particle multiplicity density in Xe–Xe collisions at sqrt(s_NN) = 5.44TeV, Phys.Lett.B 790 (2019) 35-48
[3] Javier L. Albacete: Particle multiplicities in Lead-Lead collisions at the LHC from non-linear evolution with running coupling, Phys.Rev.Lett. 99 (2007) 262301
[4] Dmitri Kharzeev, Eugene Levin, Marzia Nardi: Color glass condensate at the LHC: Hadron multiplicities in pp, pA and AA collisions, Nucl.Phys.A 747 (2005) 609-629

Datum zadání: 20.10.2022

Datum odevzdání: 15.08.2023

Výzkumný úkol odevzdá student v elektronické podobě nahráním souboru ve formátu pdf do příslušné události v systému Indico. Vedoucí úkolu přiloží své písemné vyjádření k práci studenta s doporučením pro hodnocení.

..... garant programu

..... vedoucí katedry

Prohlášení

Prohlašuji, že jsem tento výzkumný úkol vypracovala samostatně a použila jsem pouze podklady (literaturu, projekty, SW atd.) uvedené v přiloženém seznamu.

Nemám závažný důvod proti použití tohoto školního díla ve smyslu § 60 Zákona č. 121/2000 Sb., o právu autorském, o právech souvisejících s právem autorským a o změně některých zákonů (autorský zákon).

V Praze dne .....

.....
Helena Hesounová

Acknowledgements

I thank my supervisor, prof. Jesús Guillermo Contreras Nuño, Ph.D. of the Department of Physics, Faculty of Nuclear Sciences and Physical Engineering, Czech Technical University in Prague, for his guidance and patience. In addition, I have to express my gratitude to my colleagues Ing. Tomáš Herman and Ing. Diana Krupova for their advice and support. Lastly, I thank prof. David Dobrigkeit Chinellato, Ph.D., member of the ALICE Collaboration, for his help with the O^2 software.

Helena Hesounová

Název práce:

Měření multiplicity ve srážkách těžkých iontů v rámci experimentu ALICE v průběhu LHC Run 3

Autor: Helena Hesounová

Studijní program: Aplikace přírodních věd
Obor: Jaderná a částicová fyzika
Druh práce: Výzkumný úkol

Vedoucí práce: prof. Jesús Guillermo Contreras Nuño, Ph.D.
Katedra fyziky, Fakulta jaderná a fyzikálně inženýrská, České vysoké učení technické v Praze

Abstrakt: Velký hadronový urychlovač byl 5. Června 2022 spuštěn pro Run 3 po období Long Shutdown 2 (LS2). V době LS2 byl experiment ALICE vylepšen, díky čemuž jsou detektory nyní schopné nepřerušovaného vyčítání dat, a byl vytvořen nový software pro Online-Offline analýzu. Nové uspořádání experimentu a nový software umožňují přesnější měření multiplicity ve srážkách těžkých iontů. Tato práce obsahuje základní analýzu nejnovějších dat ze srážek olovo–olovo.

Klíčová slova: LHC, ALICE, multiplicita ve srážkách těžkých iontů

Title:

Measurement of multiplicity in heavy-ion collisions with ALICE during the LHC Run 3

Author: Helena Hesounová

Study program: Application of Natural Sciences
Specialization: Nuclear and Particle Physics

Supervisor: prof. Jesús Guillermo Contreras Nuño, Ph.D.
Department of Physics, Faculty of Nuclear Sciences and Physical Engineering, Czech Technical University in Prague

Abstract: On the 5th of July 2022, the LHC Run 3 started after the Long Shutdown 2 (LS2) period. During the LS2 period, the ALICE experiment underwent an upgrade of its detectors, which are now capable of continuous readout, and the new Online-Offline analysis software, also called O^2 software, was developed. The new setup and software allow for higher precision of multiplicity measurements in heavy-ion collisions. A simple analysis of the latest lead–lead data is provided in this thesis.

Key words: LHC, ALICE, multiplicity in heavy-ion collisions

Contents

Preface

The LHC Run 3 began on the 5th of July 2022, and the upgraded detector complex of ALICE has acquired the first lead–lead collision data of the new Run on the 18th of November 2022 at the center-of-mass energy of $\sqrt{s_{\mathrm{NN}}} = 5.36$ TeV. In this report, these new data are analyzed using the new Online-Offline (O^2) software. The analysis script was run over data on the Grid using the ALICE system called Hyperloop.

Before discussing the analysis, a short outlook of the ALICE detector and its upgrade during the Long Shutdown 2 period is given in Chapter 1 along with an introduction to the structure of the O^2 software.

Chapter 2 focuses on the Color Glass Condensate (CGC) model of particle production in heavy-ion collisions. The Balitsky-Kovchegov equation and its extension using the running-coupling constant, based on Ref. [1], is discussed in Section 2.1. The Color Glass Condensate approach by Khazareev, Levin, and Nardi (Ref. [2]) is the focus of Section 2.2.

A summary of previous measurements of lead–lead and xenon–xenon collisions done with ALICE, based on Ref. [3] and Ref. [4] respectively, is given in Chapter 3.

The last chapter, Chapter 4, contains my analysis of the lead–lead data LHC22s and corresponding Monte Carlo simulations LHC22i1 and LHC22k3b2. The event selection criteria are listed, and vertex reconstruction, momentum distributions, and multiplicity results are shown.

The report ends with a summary and the outlook of the next steps of this work.

Chapter 1

LHC and ALICE

The currently most advanced high-energy physics laboratory in the world lies on the Franco-Swiss border and is called the CERN complex. It consists of many accelerators and experiments. The latest addition is the Large Hadron Collider (LHC) which produced its first data in 2008.

This ring accelerator is capable of colliding protons and heavy ions at the center-of-mass energy up to $\sqrt{s} = 14$ TeV and $\sqrt{s}_{\mathrm{NN}} = 5.52$ TeV, respectively Ref. [5]. These energies are the highest possible for the current collider, but they have not been reached yet. The currently highest ones reached are $\sqrt{s} = 13.6$ TeV and $\sqrt{s}_{\mathrm{NN}} = 5.36$ TeV, respectively. The LHC uses the older complex for pre-acceleration. There are four interaction points where the collisions may happen, and there is an experiment at each one of them. One of the experiments is ALICE (A Large Ion Collider Experiment), which is the main focus of this thesis.

The whole complex operates in Runs, periods of data taking usually lasting three years, followed by a so-called Long Shutdown period (LS), which serves for repairs and upgrades. In this report, the interest is in Run 2 (2015 to 2018), the following Long Shutdown 2 (2019 to 2021), and the data from Run 3 (started in July 2022). Fig. 1.1 shows more details about the long-term plan for the LHC.

This chapter is not a complete overview of the structure and the upgrade of the ALICE experiment. Only detectors, which are relevant to the measurements discussed in Chapter 4, are mentioned here. A more thorough description was provided in my Bachelor thesis Ref. [7], and the origin of most information are Ref. [8] and Ref. [9]. The first part of this chapter is dedicated to the ALICE detector during Run 2, the second part describes the upgrade of ALICE during LS2, and the third part focuses on a new analysis software called O^2.

1.1 ALICE during Run 2

The ALICE experiment is very complex and consists of many different detectors. The schema of the ALICE detector during Run 2 is in Fig. 1.2. The main components are the Inner Tracking System (ITS), the Time Projection Chamber (TPC),

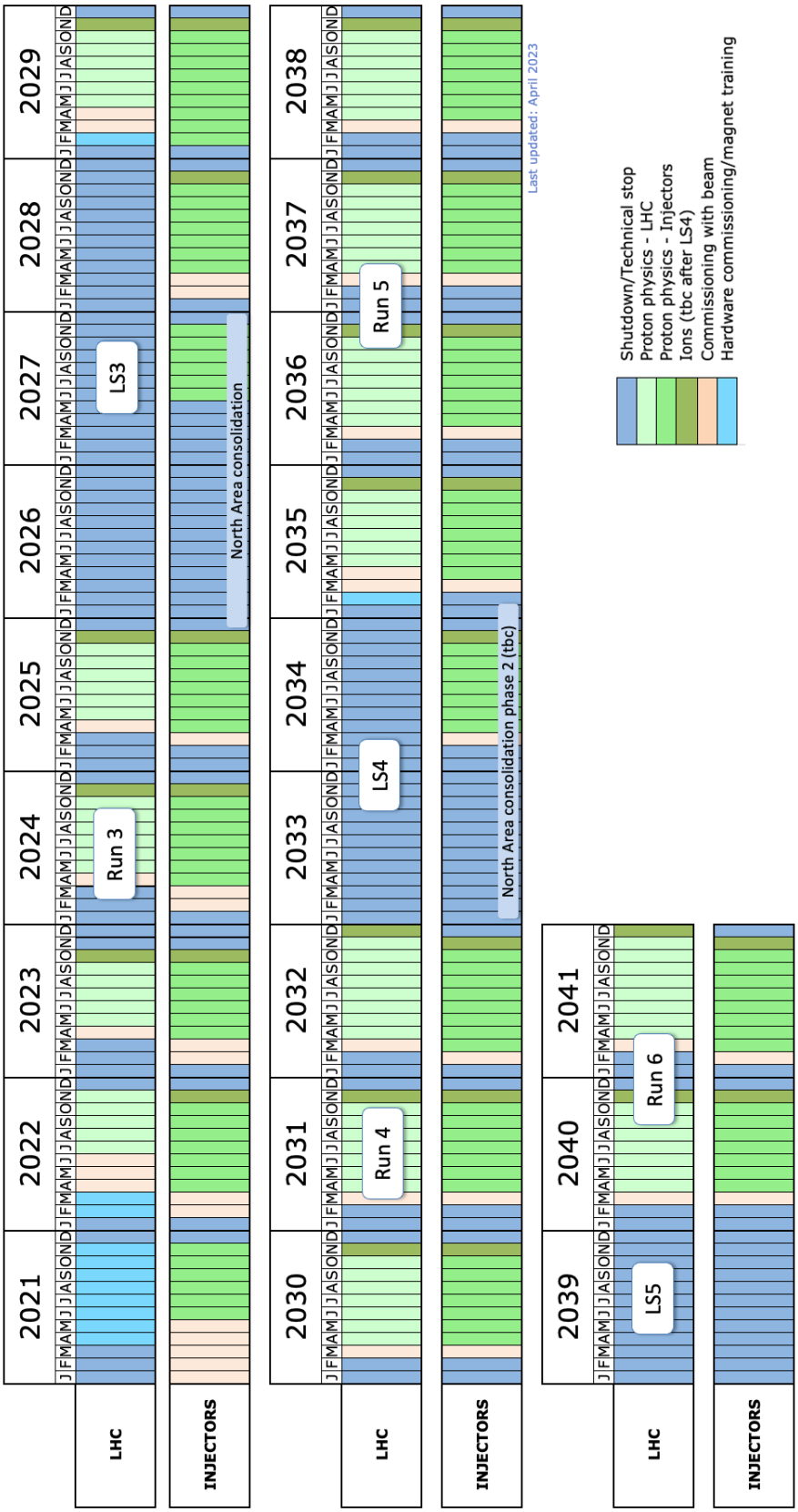

Figure 1.1: The long-term plan of the LHC. Last updated in April 2023. Taken from Ref. [6].

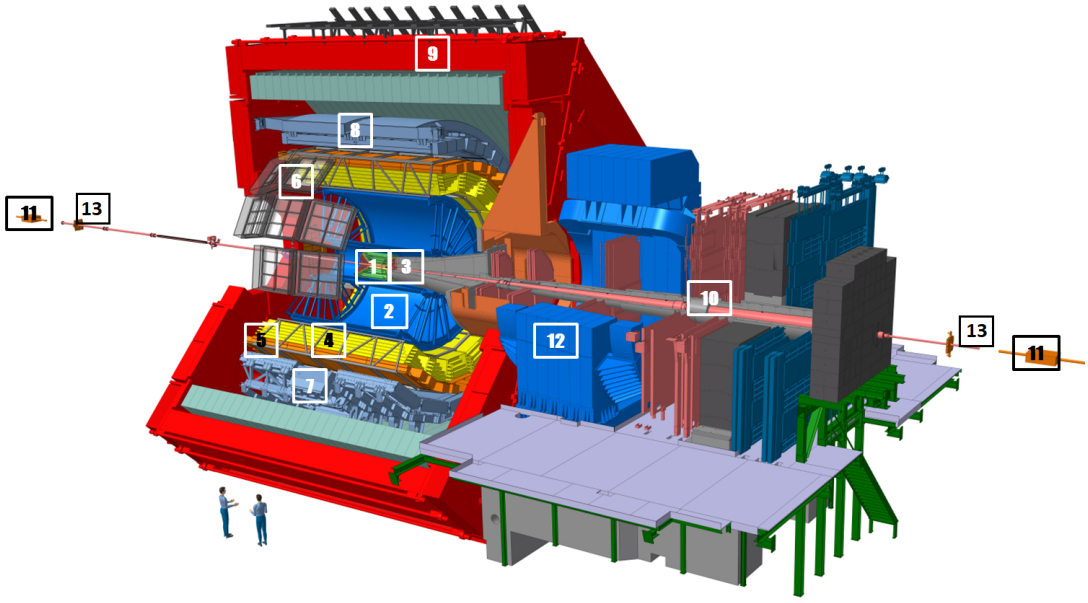

Figure 1.2: The schema of ALICE experiment during Run 2. (1) ITS, (2) TPC, (3) T0, V0, FMD, (4) TRD, (5) TOF, (6) HMPID, (7) PHOS, (8) EMCal, (9) L3 Magnet, (10) Muon tracker, (11) ZDCs, (12) Dipole magnet, (13) AD detectors. Taken from Ref. [10] and adjusted.

the Time-of-Flight (TOF) detector, the L3 magnet, and the forward rapidity detectors: T0, V0, Forward Multiplicity Detector (FMD), and Zero Degree Calorimeters (ZDCs).

The ITS had a different structure during Run 2 than now after the upgrade. It used to consist of three silicon tracking detectors: pixel (SPD), drift (SDD), and strip (SSD), which had two layers each. The pseudorapidity coverage of the ITS was $|\eta| < 1.3$, but for the SPD, it was $|\eta| < 2$.

For this thesis, the SPD is the most important as it is the innermost detector of the whole ALICE complex, and it provides the first approximation of particle tracks, the so-called tracklets. A tracklet is a straight line created from two hits in the two layers of SPD, and it was used to make the first approximation of collision multiplicity and position of the primary vertex.

The ITS, together with the TPC, TOF, and other detectors, was placed inside a magnetic field created by the solenoidal L3 magnet, and they were used for particle tracking and charge and momentum determination. The primary vertex reconstruction precision was 100 µm. The structure of the old ITS and the placement of some of the forward detectors is shown in Fig. 1.3.

The forward detectors produced information about centrality, particle production, and spatial distribution. Moreover, they were used as minimum bias (MB) triggers. MB trigger is supposed to select an unbiased sample of events with a collision.

The ZDC, FMD, T0, and V0 detectors were placed on both sides of the detector, whereas the new FV0 detector is a one-arm detector. The pseudorapidity coverage

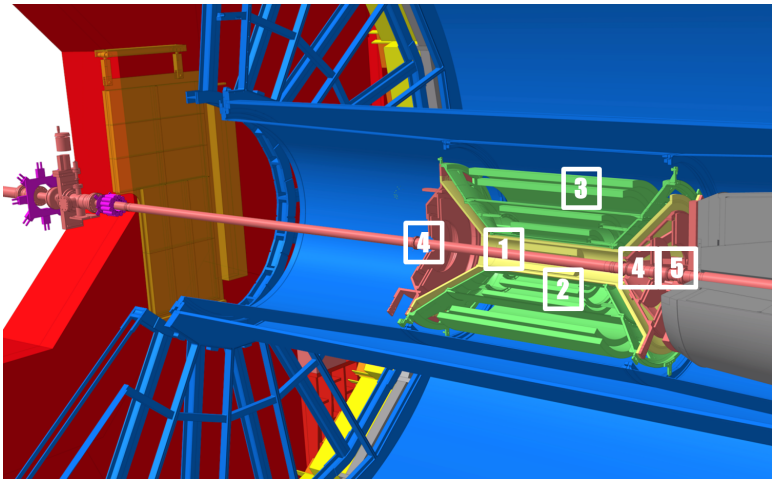

Figure 1.3: The schema of the inner part of the ALICE central barrel during Run 2. (1) SPD, (2) SDD, (3) SSD, (4) FMD, T0, (5) V0. Taken from Ref. [10] and adjusted.

for T0s was $-3.3 < \eta < -2.9$ and $4.5 < \eta < 5.0$ and for FMD $-3.4 < \eta < -1.7$ and $1.7 < \eta < 5.0$. Therefore, the FMD and ITS provided charged particle multiplicity distributions in the range $-3.4 < \eta < 5.0$.

1.2 ALICE upgrade

During the LS2 period, ALICE underwent a significant upgrade. Apart from a new ITS structure, the forward detectors were replaced by the Fast Interaction Trigger (FIT), and many other detectors were modified. The current structure of ALICE is in Fig. 1.4. This upgrade allows ALICE to increase the readout rate for lead–lead collisions from below 1 kHz up to 50 kHz Ref. [11].

The new ITS, called ITS2, now consists of seven layers of silicon tracking detectors, and it should be able to provide us with a complete track instead of just a tracklet. The seven layers are divided into an Inner Barrel (IB), which consists of the three innermost layers, and an Outer Barrel (OB), which consists of the four outer layers. The ITS2 structure and placement of new forward detectors are in Fig. 1.5.

The seven layers of the ITS2 amount to 192 staves and consist of 12.5 $\times 10^9$ CMOS Monolithic Active Pixel Sensors (MAPS). The maximum coverage of the ITS2 as a whole is $|\eta| < 1.22$, the spatial resolution of pixel chips is 5 µm, and the detection efficiency is higher than 99 % Ref. [12].

Three detectors in the forward regions are now, after the upgrade, collectively called Fast Interaction Trigger (FIT). Their purpose includes providing minimum bias (MB) triggering, luminosity monitoring, collision time measurement, centrality determination, and distinguishing diffractive or ultra-peripheral events Ref. [13].

FIT is composed of Cherenkov detectors (FT0s) and Forward Diffractive Detectors (FDDs) in both forward directions and of a scintillator disk (FV0) on one side. Their

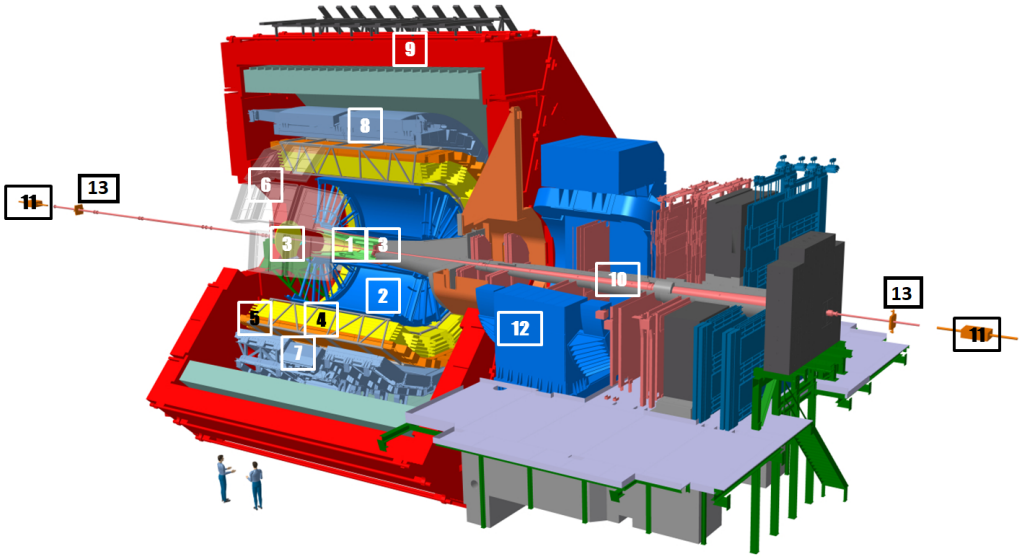

Figure 1.4: The schema of ALICE experiment during Run 3. (1) ITS, (2) TPC, (3) FT0 (left and right), FV0 (left), (4) TRD, (5) TOF, (6) HMPID, (7) PHOS, (8) EMCal, (9) L3 Magnet, (10) Muon tracking chambers, (11) ZDCs, (12) Dipole magnet, (13) FDD detectors. Taken from Ref. [10] and adjusted.

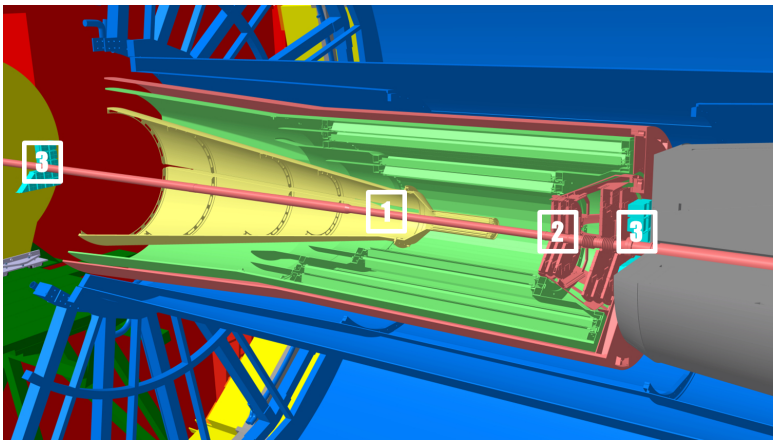

Figure 1.5: The schema of the inner part of the ALICE central barrel during Run 3. (1) ITS, (2) MFT, (3) FT0-A (left), FT0-C (right). Taken from Ref. [10] and adjusted.

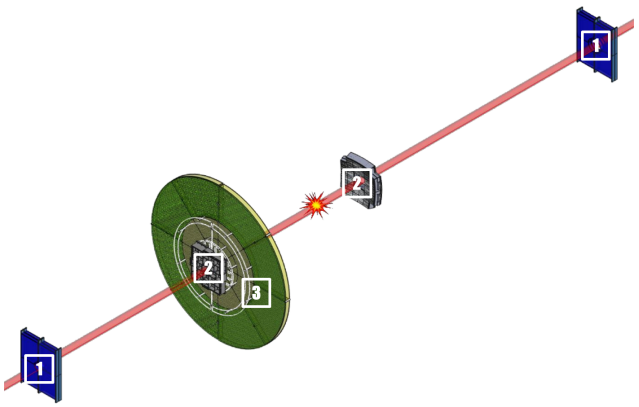

Figure 1.6: The schema of FIT during Run 3. (1) FDDs, (2) FT0s, (3) FV0. Taken from Ref. [13] and adjusted.

setup is shown in Fig. 1.6. The FIT system has a time resolution better than 40 ps.

The FT0s have a pseudorapidity coverage of $3.5 < \eta < 4.9$ and $-3.3 < \eta < -4.9$. There are 96 readout channels in FT0A and 112 in FT0C Ref. [13]. The Cherenkov radiators are attached to micro-channel plate photomultiplier tubes (MCP-PMTs). These detectors, for a single minimum ionization particle (MIP), have a time resolution better than 50 ps, and they are placed at 3.3 m and -0.819 m from the nominal interaction point.

The FV0 detector, composed of a plastic scintillator ring, is segmented into five concentric rings and is placed at 3.16 m from the nominal interaction point. In total, it has 48 readout PMT channels, which are connected to the plastic scintillator using optical fibers. The time resolution of FV0 is between 200 and 250 ps, and the pseudorapidity coverage is $2.2 < \eta < 5.0$. Its purpose is to determine the collision event plane and centrality.

The FDD detector consists of two plastic scintillator arrays with a total of 16 readout channels. One array is placed at 17 m from the nominal interaction point, and the other is at -19 m. They cover $4.8 < \eta < 6.3$ and $-7.0 < \eta < -4.9$. The time resolution of FDD is well below 1 ns.

1.3 Online-offline analysis software

The upgrade of LHC and ALICE brought a significant increase in the readout and interaction rates. Moreover, many of the new ALICE detectors have a continuous readout. These are the two main reasons why a new analysis software was needed for Run 3. In this section, an overview of the new software is given. More information about its origin was provided in my Bachelor Thesis Ref. [7], and a complete report is in Ref. [14].

Data are stored in root files as they were for Run 2. One of the differences is that instead of using AOD.root file names, which stands for Analysis Object Data, the files for Run 3 are called AO2D.root. Another term that stayed in use is workflow,

which means a collection of tasks to be run. The tasks can be divided into two groups: service tasks (event selection, particle identification (PID) ...) and analysis tasks (spectra ...).

Because of the continuous readout, it is no longer possible to store data per collision. A unit called Dataframe is used instead, and it can contain multiple collisions, which leads to a new definition of a collision itself. In previous measurements, collisions contained tracks, which underwent analysis and produced one primary vertex of said collision. For Run 3, the definition is a bit different. Tracks are assigned to a Dataframe, and their analysis produces multiple primary vertexes. Each separate primary vertex is what we call a collision. However, this approach gives rise to a new problem: a phenomenon called ambiguous tracks. Ambiguous tracks are tracks that were not assigned to any primary vertex or that were assigned to multiple primary vertices.

Measured data are stored using a new paradigm, and the stored data are immutable. In previous runs, data were stored in arrays of structures (aos), but in Run 3 they are stored in a structure of arrays (soa). This structure is called a table, and each array is a column. This approach is easy to picture and optimized for time-saving bulk operations. In addition, only an absolute minimum of data is stored. Any information derived from other data is not stored but created on-the-fly.

The tables are practical for handling. If they have the same number of rows, tables can be joined, and if they do not, they can still be connected via index columns or even index tables. Each table has an automatically created iterator, which can be used for looping over the table with a bulk operation instead of a for cycle.

There are four different types of columns. The basic one that stores the data is called static. A column using an expression to combine the information from static columns is called an expression column, and once calculated, it behaves like a static one. The expression column gives the same answer each time it is calculated. Another type is an index column linking different columns or tables together. Lastly, there is a dynamic column, similar to expression columns, but unlike those, it uses arguments or parameters. The values contained in the dynamic column are dependent on the input.

The whole system is built in a way that is optimized for bulk operations and minimum data storage. Examples of bulk operations are expression columns, looping over tables using iterators, filtering, and partitioning tables using the filter and partition functions instead of if and for clauses. If and for clauses still can be used, though their use is discouraged.

The structure of an analysis task, written in C++, is the following. First, all the used header files and namespaces need to be stated. Then there has to be at least one Struct containing an init function and an arbitrary number of processes. When more than one process is present, a switch has to be added. At the end of the task, there must be a WorkflowSpec function.

When running a task, the command has to contain all the tasks and needed helper tasks; they can be provided in an arbitrary order separated using a pipe. Moreover,

an input AO2D.root file has to be specified.

To conclude, to analyze data from LHC Run 3, new software was needed. This new software, the Online-Offline analysis system (O^2), is optimized for bulk operations and fast data processing. Only a minimum of data is stored, and the original data is immutable.

Chapter 2

Models of particle production in heavy-ion collisions

To better understand the inner workings of the universe, scientists design experiments to measure different properties of nature. These measured properties are then described using models.

In this thesis, the model of Color Glass Condensate (CGC) is discussed in the context of using it to predict the multiplicity of created particles in a hadron collision. Two different approaches are used. One is based on the running coupling Balitsky-Kovchegov (BK) equation and is the main focus of Sec. 2.1, which is a summary of Ref. [1]. The other approach is based on Ref. [2] and is described in Sec. 2.2.

2.1 A model based on the running-coupling Balitsky-Kovchegov equation

The equations of quantum chromodynamics (QCD) can be, for small enough coupling constant α_s, expanded into a Taylor-like series. The first few terms of that expansion serve as a good enough approximation. This approximation is called perturbative quantum chromodynamics (pQCD), and at high energies, it describes the behavior of gluons. To describe a gluon scattering, an infinite set of equations, called the Color Glass Condensate equations or the B-JIMWLK equations, is used. When the large N_c (number of colors) limit is applied, the infinite set of equations is reduced to a single, non-linear equation called the Balitsky-Kovchegov equation.

In this section, the numerical implementation of k_t-faktorization with running coupling Balitsky-Kovchegov unintegrated gluon distributions is summarized, and a comparison of this model to multiplicity measurements of collisions at the LHC, specifically from ALICE and CMS, is shown.

A model based on running-coupling BK unintegrated gluon distributions is to be used for predictions for the centrality dependence of certain observables in heavy-ion, proton–proton, and ion–proton collisions, such as charged particle multiplicity

or transverse momenta. In addition, it can be used to obtain initial conditions for hydrodynamic simulations of heavy-ion collisions.

2.1.1 Multiplicity distribution

Based on the paper from Javier L. Albacete and Adrian Dumitru Ref. [1], when the k_t factorization is applied, the formula for charged particle multiplicity distribution is as follows:

$$\frac{dN_{\rm ch}}{dy} = \frac{2}{3}\kappa_g \int d^2R \int d^2p_t \, \frac{dN^{A+B\to g}}{dy\, d^2p_t\, d^2R}, \tag{2.1}$$

where R is the transverse coordinate and the "gluon multiplication factor" $\kappa_g = 5$ is determined empirically. The upper limit of the integral over the gluon transverse momentum was set as $p_t^{max} = 12$ GeV because a higher value would need a correction of the gluon multiplication factor. The number of gluons produced per unit rapidity at R in an A+B collision is given by

$$\frac{dN^{A+B\to g}}{dyd^2p_td^2R} = \frac{1}{\sigma_s}\frac{d\sigma^{A+B\to g}}{dyd^2p_td^2R}. \tag{2.2}$$

σ_s is the effective interaction arrea and $\frac{d\sigma^{A+B\to g}}{dyd^2p_td^2R}$ is the cross-section for an inclusive gluon production in this A+B collision and is given by

$$\frac{d\sigma^{A+B\to g}}{dy\, d^2p_t\, d^2R} = K\,\frac{2}{C_F}\frac{1}{p_t^2}\int^{p_t}\frac{d^2k_t}{4}\int d^2b\,\alpha_s(Q)\,\varphi(\frac{|p_t+k_t|}{2},x_1;b)\,\varphi(\frac{|p_t-k_t|}{2},x_2;R{-}b), \tag{2.3}$$

where $K \approx 2$ is a normalisation factor aquired from proton–proton collision data at $\sqrt{s} = 7$ TeV, $C_F = \frac{N_c^2-1}{2N_c}$, k_t is the gluon transverse momentum and p_t is the transverse momentum of the original object, φ is the unintegrated gluon distribution (ugd) and $x_{1,2} = (p_t/\sqrt{s})\exp(\pm y)$.

The ugd φ in Eq. 2.3 is, through its Fourier transform, related to the dipole scattering amplitude in the adjoint representation $\mathcal{N}_G$:

$$\varphi(k,x,b) = \frac{C_F}{\alpha_s(k)\,(2\pi)^3}\int d^2\mathbf{r}\; e^{-i\mathbf{k}\cdot\mathbf{r}}\,\nabla^2_{\mathbf{r}}\mathcal{N}_G(r,Y{=}\ln(x_0/x),b), \tag{2.4}$$

which is related to the quark dipole scattering amplitude $\mathcal{N}$ as follows:

$$\mathcal{N}_G(r,x) = 2\mathcal{N}(r,x) - \mathcal{N}^2(r,x). \tag{2.5}$$

The quark dipole scattering amplitude $\mathcal{N}$ is the solution of the Balitsky-Kovchegov equation:

$$\frac{\partial \mathcal{N}(r,x)}{\partial \ln(x_0/x)} = \int d^2\underline{r}_1 K(\underline{r},\underline{r}_1,\underline{r}_2)\left[\mathcal{N}(r_1,x)+\mathcal{N}(r_2,x)-\mathcal{N}(r,x)-\mathcal{N}(r_1,x)\mathcal{N}(r_2,x)\right], \tag{2.6}$$

where K is the evolution kernel, $\underline{r}_2 = \underline{r} - \underline{r}_1$ and $\underline{r} = \underline{x} - \underline{y}$ are the dipoles transverse sizes and x_0 is the starting point of the evolution. In this equation, translational invariance is assumed. Therefore, the dipole amplitude does not depend on the impact parameter.

To acquire the running-coupling BK (rcBK) equation, a running-coupling evolution kernel has to be used:

$$K^{\mathrm{run}}(\mathbf{r},\mathbf{r_1},\mathbf{r_2}) = \frac{N_c\,\alpha_s(r^2)}{2\pi^2}\left[\frac{1}{r_1^2}\left(\frac{\alpha_s(r_1^2)}{\alpha_s(r_2^2)}-1\right)+\frac{r^2}{r_1^2\,r_2^2}+\frac{1}{r_2^2}\left(\frac{\alpha_s(r_2^2)}{\alpha_s(r_1^2)}-1\right)\right]. \tag{2.7}$$

The initial condition (i.c.) for the rcBK equation is given by

$$\mathcal{N}(r,Y=0;R) = 1-\exp\left[-\frac{(r^2\,Q_{s0}^2(R))^\gamma}{4}\ln\left(\frac{1}{\Lambda\,r}+e\right)\right], \tag{2.8}$$

where $Q_{s0}(R)$ is the initial saturation scale at R, Λ is the QCD scale parameter, and γ is the so-called anomalous dimension. In the Ref. [1], $\Lambda = 0.241$ GeV and $x_0 = 0.01$. The value of $\gamma = 1$ corresponds to the McLerran-Venugopalan model, and with $Q_{s0}^2 = 0.2$ GeV^2 is labeled MV i.c. in the figures below. For a better data description, another set of initial conditions, labeled MV$^{\gamma=1.119}$ i.c, was used, with the parameter $\gamma = 1.119$ and $Q_{s0}^2 = 0.168$ GeV^2. The difference in steepness for a single nucleon case and three different values of the initial saturation scale Q_{s0} is shown in Fig. 2.1.

2.1.2 Comparison to data and predictions

A translation from rapidity to pseudorapidity distributions is required to compare the model with data . This translation is given by

$$\frac{dN_{\mathrm{ch}}}{d\eta} = \frac{\cosh\eta}{\sqrt{\cosh^2\eta + m^2/P^2}}\,\frac{dN_{\mathrm{ch}}}{dy}. \tag{2.9}$$

Comparison of the centrality dependence of the charged particle multiplicity acquired from MV$^{\gamma=1.119}$ i.c., and MV i.c. and ALICE data for lead–lead collisions at $\sqrt{s} = 2.76$ TeV is shown in Fig. 2.2. From this figure, it is not evident that MV$^{\gamma=1.119}$ i.c. describes the data better than basic MV i.c. However, when compared to the transverse momentum distribution from CMS, the better accuracy of MV$^{\gamma=1.119}$ i.c. becomes evident (Fig. 2.3).

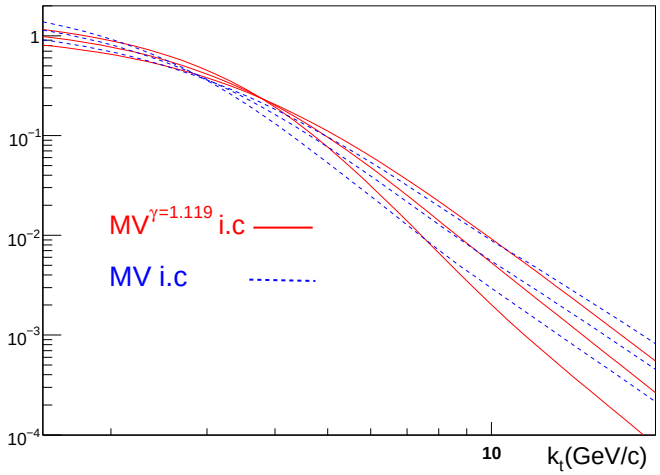

Figure 2.1: UGD's for the two different initial conditions in the single nucleon case: $\mathrm{MV}^{\gamma=1.119}$ (solid) and MV (dashed) at rapidities $Y = \ln(x_0/x) = 1.5$, 3 and 6. Taken from Ref. [1].

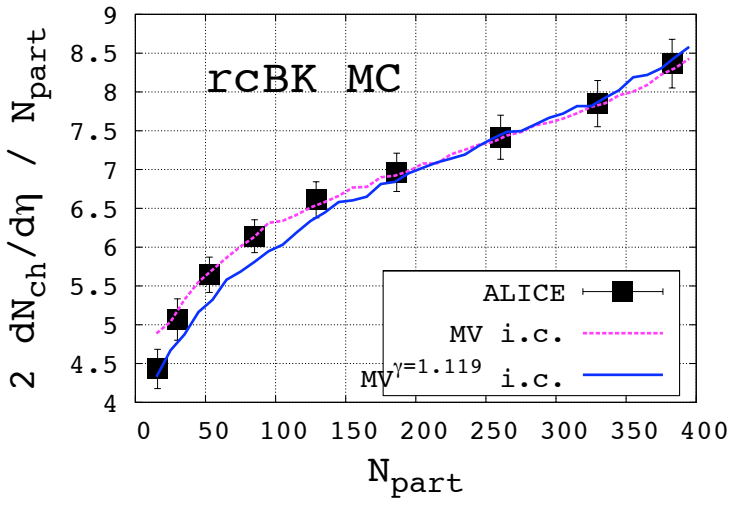

Figure 2.2: Centrality dependence of the charged particle multiplicity at midrapidity for lead–lead collisions at $\sqrt{s} = 2.76$ TeV (ALICE data). Taken from Ref. [1].

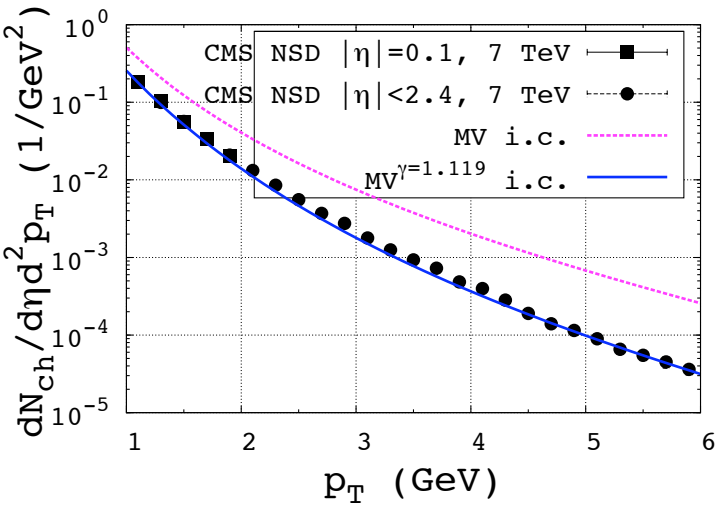

Figure 2.3: Transverse momentum distribution of charged particles at $\eta = 0$ for proton–proton collisions at $\sqrt{s} = 7$ TeV (CMS data). Taken from Ref. [1].

2.1.3 Summary

A model based on the rcBK equation can be used to predict the centrality dependence of observables. It can also be used to obtain initial conditions for hydrodynamic simulations of nucleus–nucleus collisions. The model implements a running α_s constant into the kernel of the Balitsky-Kovchegov equation. A set of initial conditions is needed. In this study, two different conditions are used: the MV i.c. and the MV$^{\gamma=1.119}$ i.c., where the latter gives more accurate predictions compared to data.

To calculate the multiplicity observable, a k_t factorization formalism is introduced. This formalism ties together the produced number of gluons with the effective interaction area and the cross section for inclusive gluon production. The observables are then obtained by integrating said formula.

Comparison of the model with two different sets of initial conditions with data from ALICE and CMS are shown in Figs. 2.2 and 2.3, respectively.

2.2 Color Glass Condensate approach by Kharzeev, Levin, and Nardi

This section is focused on the theory of the Color Glass Condensate approach and its application to LHC multiplicity data. We will be particularly interested in multiplicity predictions for proton–proton, proton–nucleus, and nucleus–nucleus collisions. This section is a summary of the work presented in Ref. [2].

The Color Glass Condensate is characterized by parton saturation caused by strong coherent gluon fields. It is considered an initial condition for system evolution, the

main phenomenological parameter being the saturation momentum. This approach provides us with a set of predictions for multiplicity distributions and their centrality and rapidity dependencies.

For the description of previously measured data at RHIC, there were three main assumptions used. Firstly, the inclusive parton production is at Bjorken $x \leq 10^{-2}$ driven by parton saturation in strong gluon fields from the McLerran-Venugopalan model (discussed in Sec. 2.1). Secondly, the low x region, where $\alpha_s \ll 1$ and where quantum evolution becomes important, is taken as $x \approx 10^{-3}$. Lastly, we assume that the multiplicity is not significantly affected by final state interactions, and thus the deviations from local parton hadron duality are negligible. Local parton hadron duality connects partons considered at the moment of collision with later measured hadrons.

To describe new measurements done at the LHC, where the value of Bjorken x is two orders of magnitude smaller than it was at RHIC, the JIMWLK or the Balitsky-Kovchegov equation (discussed in Sec. 2.1) is used to deal with high parton density QCD. However, the LHC energy is still not high enough to omit pre-asymptotic corrections. Therefore, the next-to-leading order (NLO) correction is added to the leading-order (LO) equations.

2.2.1 Geometry of collisions

One of the approximations used in many models is taking a straight line as the path of colliding nucleons. The centrality of a nucleus–nucleus (or proton–nucleus) collision is parametrized by the number of participants N_{part}, which counts all nucleons that participate in at least one inelastic collision. This number is deduced by counting all the spectator nucleons in the forward rapidity region. Both these numbers depend on the impact parameter b or its proxy, centrality. These calculations are done using nuclear thickness functions T_A. For proton–nucleus collisions, one thickness function is replaced by a delta function.

2.2.2 The General Formula

The general formula for the inclusive particle production used in this paper is:

$$E\frac{d\sigma}{d^3p} = \frac{4\pi N_c}{N_c^2 - 1}\frac{1}{p_t^2}\int^{p_t} dk_t^2 \alpha_s \varphi_{A_1}(x_1, k_t^2)\varphi_{A_2}(x_2, (p-k)_t^2), \tag{2.10}$$

where $x_{1,2} = (p_t/\sqrt{s})\exp(\mp y)$ and $\varphi_{A_1,A_2}(x_1, k_t^2)$ are the unintegrated gluon distributions of nuclei and N_c denotes the number of colours. This integration is divided into three regions using the minimum and maximum saturation momenta - $Q_{s,min}$, $Q_{s,max}$. These values take the minimum (maximum) of the saturation momenta of each nucleus $Q_s(A_{1,2})$.

The multiplicity distribution is than obtained by integrating Eq. 2.10 over p_t:

$$\frac{dN}{dy} = \frac{1}{S}\int d^2p_t E\frac{d\sigma}{d^3p}. \tag{2.11}$$

The S is the inelastic cross-section. When the $E\frac{d\sigma}{d^3p}$ from Eq. 2.10 is put in Eq. 2.11, one obtains

$$\frac{dN}{dy} = \frac{1}{S}\frac{4\pi N_c\alpha_s}{N_c^2-1}\times\int\frac{dp_t^2}{p_t^2}\left(\varphi_{A_1}(x_1,p_t^2)\int^{p_t^2}dk_t^2\varphi_{A_2}(x_2,k_t^2)+\right.$$
$$\left.+\,\varphi_{A_2}(x_2,p_t^2)\int^{p_t^2}dk_t^2\varphi_{A_1}(x_1,k_t^2)\right) = \frac{1}{S}\frac{4\pi N_c\alpha_s}{N_c^2-1}\int_0^\infty\frac{dp_t^2}{p_t^4}xG_{A_2}(x_2,p_t^2)xG_{A_1}(x_1,p_t^2), \tag{2.12}$$

where the second expression is obtained by integrating by parts and using the prescription for gluon density given by

$$xG(x,Q^2) = \int^{Q^2}dk_t^2\varphi(x,k_t^2). \tag{2.13}$$

The p_t integration in Eq. 2.11 and Eq. 2.12 can be divided into three regions. The first region is given by a condition: $p_t < Q_{s,min}$. It is where parton densities for both nuclei are in the saturation region. The second region, given by $Q_{s,min} < p_t < Q_{s,max}$, is where one nucleus is in the saturation region, but the second one is in the DGLAP evolution region. The last region is given by: $p_t > Q_{s,max}$, where both nuclei are in the DGLAP evolution region.

2.2.3 Predictions and comparison to measurements

The next part of Chapter 2 focuses on the predictions for proton–proton collisions and their correspondence to previous measurements. In general, proton–proton or proton–antiproton collisions contain a specific problem arising, among others, from the unknown geometrical properties of a nucleon. Another difficulty is the non-negligible effect of the non-perturbative corrections due to the small value of the saturation momentum.

Figure 2.4 shows the multiplicity distribution for different energies compared to previously measured data. The model describes experimental data more accurately for lower energies. The dependence of total multiplicity on energy for proton–proton collisions is plotted in Fig. 2.5, where the dotted line marks the expected LHC energy.

Figure 2.6 shows the pseudorapidity density for proton–proton collision compared to the pseudorapidity density per nucleon pair for nucleus–nucleus collisions. The dotted lines again mark the expected LHC energy values, where the lower (higher) value is for nucleus–nucleus (proton–proton) collisions.

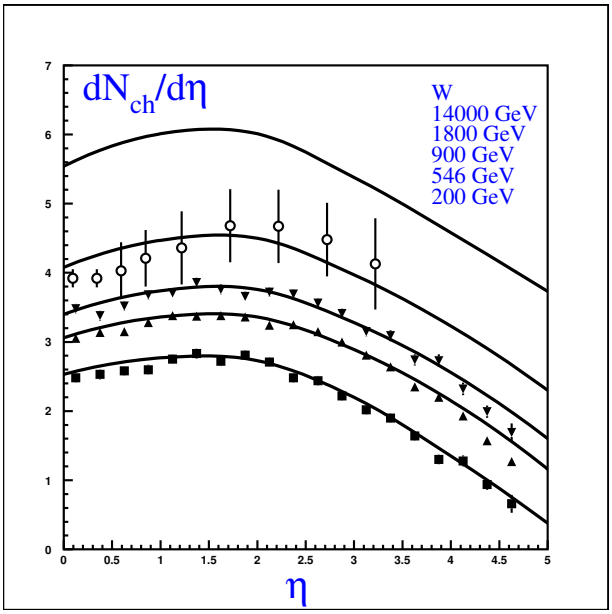

Figure 2.4: Rapidity dependence $\mathrm{d}N/\mathrm{d}\eta$ of charged hadron multiplicities in proton–proton (antiproton) collisions as a function of the pseudorapidity at different energies. Taken from Ref. [2].

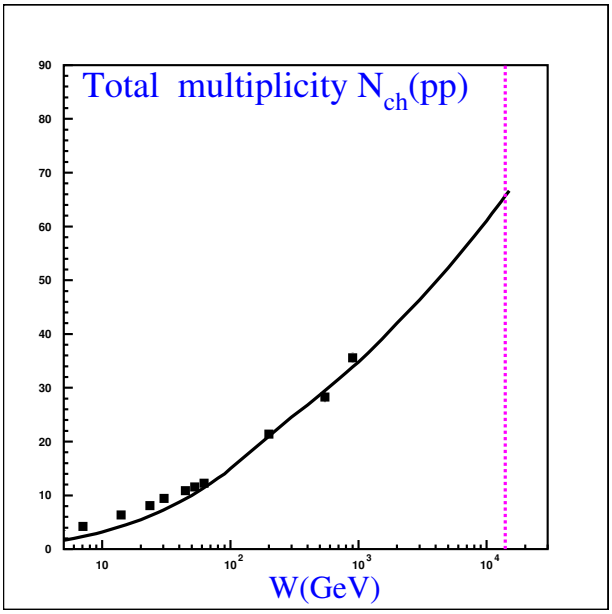

Figure 2.5: Energy dependence of total multiplicity in proton–proton (antiproton) collisions. The vertical dotted line marks the LHC energies for proton–proton collisions ($W = 14000\,GeV$). Taken from Ref. [2].

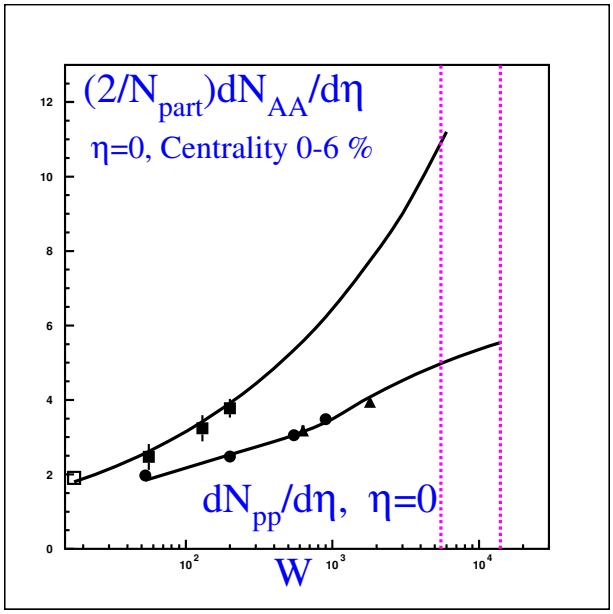

Figure 2.6: Energy dependence of charged hadron multiplicity $\mathrm{d}N/\mathrm{d}\eta$ at $\eta = 0$ in proton–proton (antiproton) collisions and of charged hadron multiplicities per participant pair $(2/N_{part})\mathrm{d}N/\mathrm{d}\eta$ at $\eta = 0$ for central nucleus–nucleus collisions. The vertical dotted lines mark the LHC energies for nucleus–nucleus collisions ($W = 5500$ GeV) and for proton–proton collisions ($W = 14000$ GeV). Taken from Ref. [2].

The multiplicity distribution prediction for lead–lead collisions is shown in Fig. 2.7, where solid (dotted) lines correspond to predictions without (with) the running QCD coupling. The red area corresponds to minimal bias events.

Figure 2.8 shows the pseudorapidity density per nucleon pair dependent on N_{part} for different pseudorapidity cuts where solid (dotted) lines correspond to predictions without (with) the running QCD coupling.

Predicted multiplicity distributions for proton–lead collisions for different centrality classes are in Fig. 2.9.

Figure 2.10 shows a comparison with other models. Note that for lower pseudorapidity region HIJING model predicts higher values for pseudorapidity density per event than this CGC model, but in the region approximately from 6 to 8, they start to coincide.

2.2.4 Summary

The model by Kharzeev, Levin, and Nardi provided us with a set of predictions for multiplicity distributions in proton–proton, proton–nucleus, and nucleus–nucleus collisions. Unlike other models, this model does not expect a large dependency of multiplicity on energy and predicts multiplicity to be rather low. However, the uncertainties of these predictions are high: around 15% for nucleus–nucleus collisions and up to 50% for proton–proton collisions. In the following sections, this CGC model is referred to as KLN or Kharzeev *et al.*

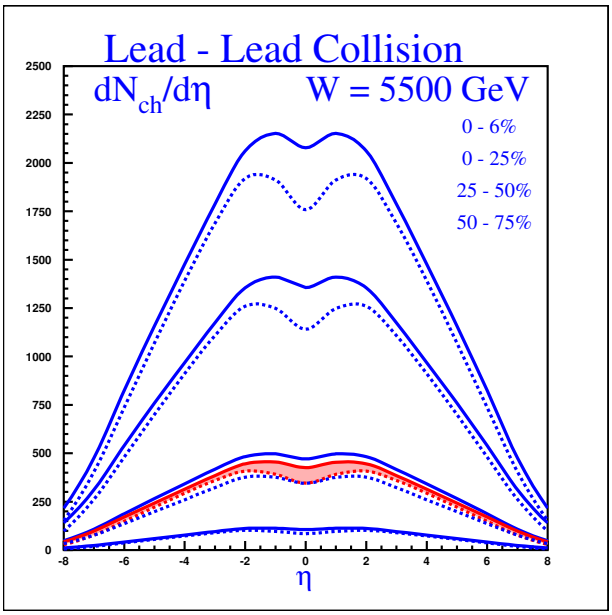

Figure 2.7: Rapidity dependence of $\mathrm{d}N/\mathrm{d}\eta$ in lead–lead collisions at the LHC energy at different centrality cuts. The solid (dotted) lines show the predictions without (with) using the running QCD coupling, respectively. The shaded area shows the prediction for the minimal bias event. Taken from Ref. [2].

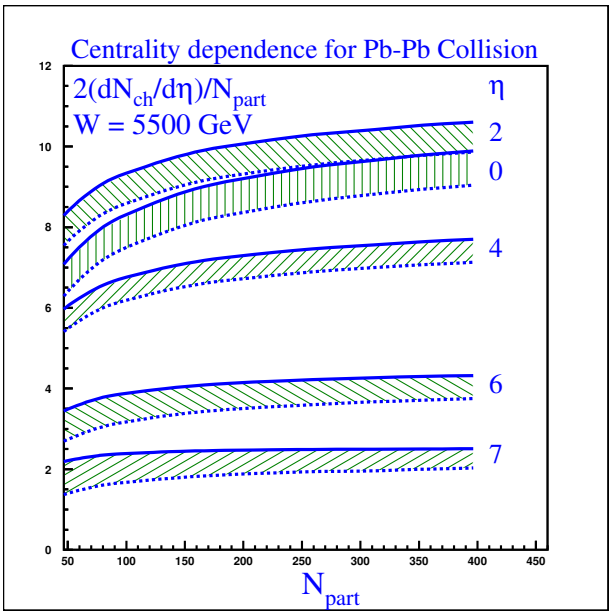

Figure 2.8: N_{part} dependence of $(2/N_{ch})\mathrm{d}N/\mathrm{d}\eta$ for lead–lead collisions at the LHC energy at different rapidity cuts. The solid (dotted) lines correspond to the prediction without (with) using the running QCD coupling, respectively. The shadowed areas show the spread of predictions. Taken from Ref. [2].

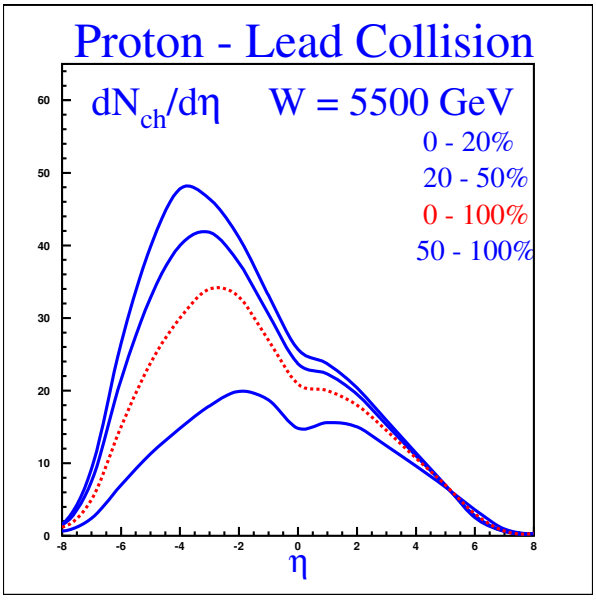

Figure 2.9: Rapidity dependence of $\mathrm{d}N/\mathrm{d}\eta$ in proton–lead collisions at the LHC energy at different centrality cuts. The dotted line corresponds to the minimal bias event. Taken from Ref. [2].

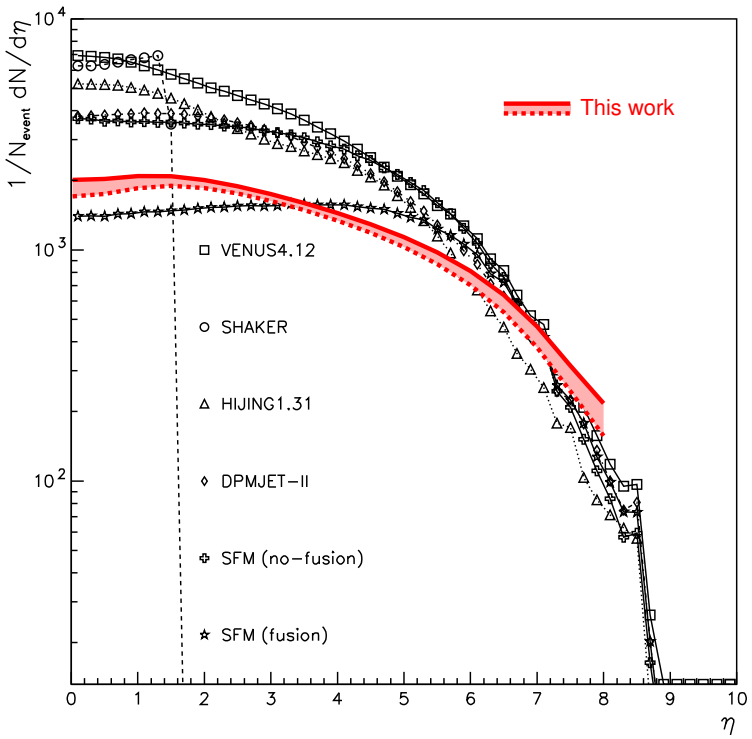

Figure 2.10: A comparison of our predictions for charged hadron multiplicities in central ($b \leq 3$ fm) lead–lead collisions with the results from other approaches. Taken from Ref. [2].

Chapter 3

ALICE multiplicity measurements with Run 2 data

The ALICE experiment has taken large quantities of data during Run 2. This chapter provides an overview of two articles produced by the ALICE Collaboration where the multiplicity measurements in the lead–lead Ref. [3] and the xenon–xenon Ref. [4] collisions are reported. These data are compared to previous measurements done with ALICE and CMS and proton–proton data, taken during this run, and to different models. Results for lead–lead collisions are presented in Sec. 3.1, and xenon–xenon collisions are discussed in Sec. 3.2.

3.1 Charged-particle multiplicity in Pb–Pb collisions at $\sqrt{s_{\mathrm{NN}}} = 5.02$ TeV

This section gives an overview of Ref. [3], a paper published in December 2015. It summarises the study of the centrality dependence of the charged-particle multiplicity in lead–lead collisions at a center-of-mass energy $\sqrt{s_{\mathrm{NN}}} = 5.02$ TeV, measured by ALICE. And it compares these new data with previous measurements for nucleus–nucleus collisions performed at ALICE, ATLAS, and CMS at a center-of-mass energy $\sqrt{s_{\mathrm{NN}}} = 2.76$ TeV, at the SPS and RHIC from $\sqrt{s_{\mathrm{NN}}} = 9$ to 200 GeV, and with measurements of proton–proton or proton–nucleus collisions. A comparison with different models is also provided.

3.1.1 Measurement properties and data selection

The studied data were produced in November 2015. The center-of-mass energy of $\sqrt{s_{\mathrm{NN}}} = 5.02$ TeV was the highest energy ever achieved. The measured interaction rate was around 300 Hz from all interactions and 25 Hz from hadronic interaction. The rest was background from electromagnetic processes.

To achieve approximately constant acceptance of the detectors only events with the vertex position $|z| < 7$ cm were used.

Corrections for the detector acceptance and tracklet generation efficiency, which includes low p_{T} extrapolation and background tracklets removal, were needed.

Systematic uncertainties, dependent on the collision's centrality, were caused by the trigger and event selections as well as background subtraction. Systematic uncertainties arising from the contamination from weak decays, variations in detector acceptance, and those caused by the low p_{T} extrapolation had no dependence on the collision centrality. Effects due to particle composition, pileup, and material budget were negligible. The sum of all systematic uncertainties goes from 2.6% to 7.6% for the most and the least central collisions, respectively.

3.1.2 Results

The charged particle multiplicity N_{ch} of a collision is related to the collision's geometry and energy and the initial parton density. Collisions can be classified according to their centrality, which describes the level of overlap of the colliding nuclei, and therefore is closely related to the collision geometry.

To be able to compare particle production in proton–proton and nucleus–nucleus collisions, one needs to divide the charged-particle density with the number of participating nucleon pairs $\frac{2}{\langle N_{\mathrm{part}} \rangle} \langle \mathrm{d}N_{\mathrm{ch}}/\mathrm{d}\eta \rangle$.

In Fig. 3.1 $\frac{2}{\langle N_{\mathrm{part}} \rangle} \langle \mathrm{d}N_{\mathrm{ch}}/\mathrm{d}\eta \rangle$ is plotted against the center-of-mass energy and compared to previous measurements of proton–proton, proton–antiproton, proton–nucleus, deuteron–nucleus, and nucleus–nucleus collisions. The dependence on the center-of-mass energy is fitted with a power law $a \cdot s^b$. For nucleus–nucleus collisions, the fit gives $b = 0.155 \pm 0.004$. For proton–proton collisions, it gives $b = 0.103 \pm 0.002$. The trend, established by previous measurements, is confirmed by the new data. Interestingly, the values for proton–nucleus and deuteron–nucleus collisions fall on the curve of proton–proton collisions. Therefore, the rise in particle production for nucleus–nucleus collisions is not solely from multiple collisions of participants.

Figure 3.2 shows the centrality dependence of pseudorapidity density per nucleon collision. A clear dependence of multiplicity on $\langle N_{\mathrm{part}} \rangle$ is present. In this figure, the energy dependence is also shown, as the multiplicity increases by a factor of 1.2 from lead–lead collisions at $\sqrt{s_{\mathrm{NN}}} = 2.76$ TeV to lead–lead collisions at $\sqrt{s_{\mathrm{NN}}} = 5.02$ TeV. The measurement from proton–lead collisions at $\sqrt{s_{\mathrm{NN}}} = 5.02$ TeV follows a smooth trend from lead–lead data at the same energy.

A comparison of the centrality dependence of pseudorapidity density with different data models is shown in Fig. 3.3. The used models were not re-tuned using the latest measurements. A good description of the data is provided by the Monte Carlo (MC) generator EPOS LHC, which is based on the Gribov-Regge theory. However, the MC generator HIJING, which combines perturbative QCD and soft processes, fails to describe the data. Saturation-inspired models rcBK-MC, MV (described in Sec. 2.1), give an even better description. A model that describes both the shape and

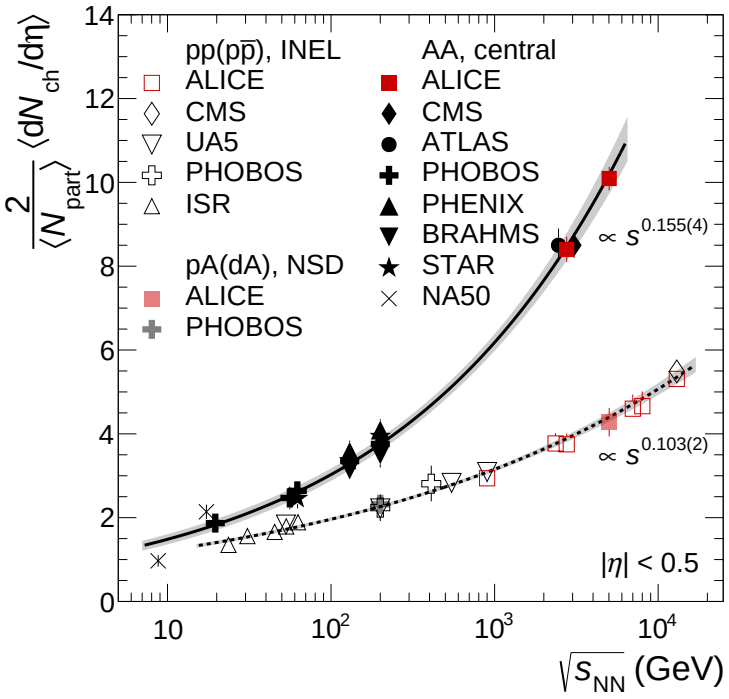

Figure 3.1: Values of $\frac{2}{\langle N_{\mathrm{part}} \rangle} \langle \mathrm{d}N_{\mathrm{ch}}/\mathrm{d}\eta \rangle$ for central lead–lead and gold–gold collisions as a function of $\sqrt{s_{\mathrm{NN}}}$. Measurements for inelastic proton–proton and proton–antiproton collisions as a function of $\sqrt{s}$ are shown along with those from non-single diffractive proton–nucleus and deuteron–nucleus collisions. The shaded bands show the uncertainties on the extracted power-law dependencies. The central lead–lead measurements from CMS and ATLAS at 2.76 TeV have been shifted horizontally for clarity. Taken from Ref. [3].

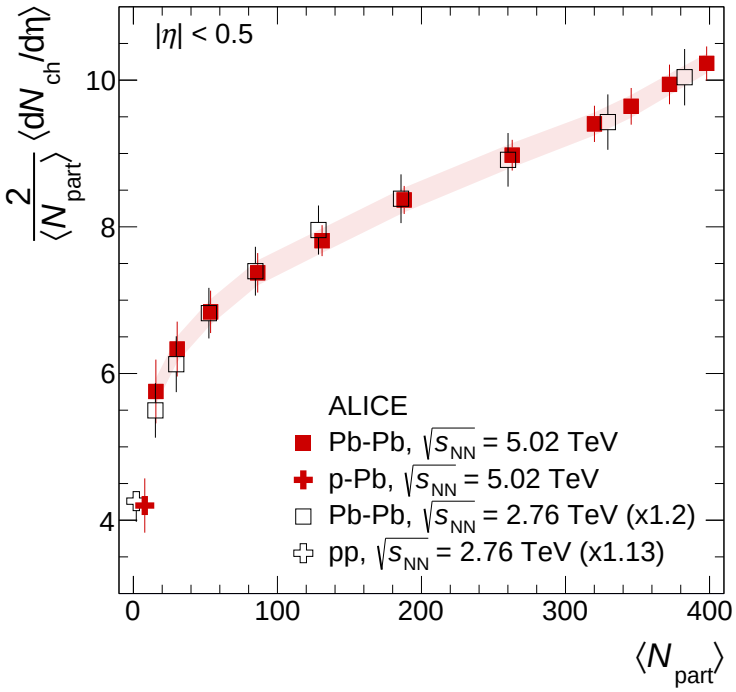

Figure 3.2: The $\frac{2}{\langle N_{\mathrm{part}}\rangle}\langle \mathrm{d}N_{\mathrm{ch}}/\mathrm{d}\eta\rangle$ for lead–lead collisions at $\sqrt{s_{\mathrm{NN}}} = 5.02$ TeV in the centrality range 0–80%, as function a of $\langle N_{\mathrm{part}}\rangle$ in each centrality class. The error bars indicate the point-to-point centrality-dependent uncertainties, whereas the shaded band shows the correlated contributions. Also shown is the result from non-single diffractive proton–lead collisions at the same $\sqrt{s_{\mathrm{NN}}}$. Data from lower energy (2.76 TeV) lead–lead and proton–proton collisions, scaled by a factor of 1.2 and 1.13, respectively, are shown for comparison. The error bars for proton–lead at $\sqrt{s_{\mathrm{NN}}} = 5.02$ TeV and lower energy lead–lead and proton–proton collisions indicate the total uncertainty. Taken from Ref. [3].

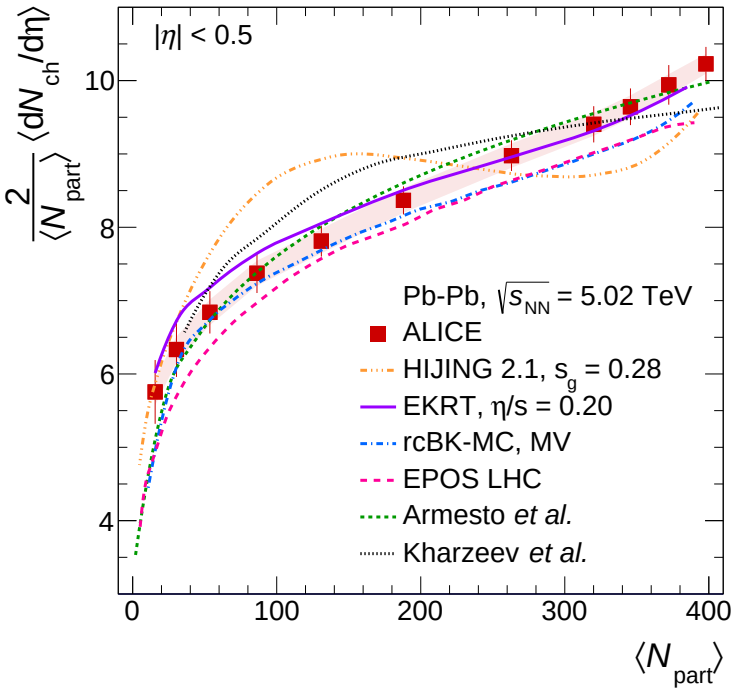

Figure 3.3: The $\frac{2}{\langle N_{\mathrm{part}}\rangle}\langle \mathrm{d}N_{\mathrm{ch}}/\mathrm{d}\eta\rangle$ for lead–lead collisions at $\sqrt{s_{\mathrm{NN}}} = 5.02$ TeV in the centrality range 0–80%, as a function of $\langle N_{\mathrm{part}}\rangle$ in each centrality class, compared to model predictions. Taken from Ref. [3].

the magnitude of the dependence is the EKRT model. This model combines gluon saturation estimation and next-to-leading order perturbative QCD. The model of Kharzeev *et al.* is presented in Sec. 2.2.

3.1.3 Summary

The measurements of pseudorapidity density at midrapidity $\langle \mathrm{d}N_{\mathrm{ch}}/\mathrm{d}\eta\rangle$ in lead–lead collisions at the center-of-mass energy of $\sqrt{s_{\mathrm{NN}}} = 5.02$ TeV has shown a 20% increase for the most central collisions compared to previous measurements done at the center-of-mass energy of $\sqrt{s_{\mathrm{NN}}} = 2.76$ TeV.

$\frac{2}{\langle N_{\mathrm{part}}\rangle}\langle \mathrm{d}N_{\mathrm{ch}}/\mathrm{d}\eta\rangle$ follows a smooth evolution with rising energy that can be fitted with a power law. The exponent of the power law is different for nucleus–nucleus collisions and proton–proton collisions. Interestingly, the proton–nucleus collisions fall on the proton–proton curve.

A majority of the models that were able to describe the data at lower energies are in good agreement with the new data.

3.2 Charged-particle multiplicity in Xe–Xe collisions $\sqrt{s_{\mathrm{NN}}} = 5.44$ TeV

An analogous analysis, as the one described in the previous section of lead–lead collisions, was done for xenon–xenon collisions at a center-of-mass energy of $\sqrt{s_{\mathrm{NN}}} = 5.44$ TeV. Said analysis, published in March of 2018 Ref. [4], is summarized in this section.

3.2.1 Measurement properties and data selection

In October 2017, the ^{129}Xe data were acquired by ALICE. The data cover a wide pseudorapidity range of $-3.5 < \eta < 5$. The rate of hadronic interaction dropped from 150 Hz at the beginning of data taking to 80 Hz at the end. Data were collected with a reduced magnetic field of 0.2 T, compared to the usual 0.5 T for lead–lead data, to increase the acceptance of low p_{T} particles.

An approximately constant acceptance is achieved for events with a primary vertex within $|z| < 7$ cm in the pseudorapidity region $|\eta| < 0.5$. Extended coverage up to $|\eta| < 2$ considers all events with primary vertex within $|z| < 20$ cm.

Uncertainties of multiplicity at mid-rapidity $|\eta| < 0.5$ arise from tracklet selection, background subtraction, particle composition, contamination by week decays, extrapolation to zero transverse momentum, and a variation in detector acceptance and efficiency. At forward rapidities, the causes of uncertainties contain correction for secondary particles, variation in rejection threshold for calculating multiplicity per event, and particle composition.

The total systematic uncertainty in $|\eta| < 2$ is 6.4%, and 2% for peripheral and central collisions, respectively. In the forward region of $\eta > 3.5$, the systematic uncertainty amounts to 6.9%, and in other forward regions, it amounts to 6.4%.

3.2.2 Results

The charged-particle multiplicity density N_{ch} is plotted as a function of pseudorapidity in Fig. 3.4 for 12 centrality classes. Data were obtained by the SPD in the mid-rapidity region, by the FMD in the forward region, and combined in the overlap region of $1.8 < |\eta| < 2$. In addition, a symmetrization over $\eta = 0$ was done.

The multiplicity normalised per participant pair $\frac{2}{\langle N_{\mathrm{part}} \rangle} \langle \mathrm{d}N_{\mathrm{ch}}/\mathrm{d}\eta \rangle$ at mid-rapidity plotted as a function of the center-of-mass energy is compared to previous measurements in Fig. 3.5 (top). It follows the trend established by previous measurements. Figure 3.5 (bottom) shows the same dependence for the total multiplicity rescaled per pair participants $\frac{2}{\langle N_{\mathrm{part}} \rangle} N_{\mathrm{ch}}^{\mathrm{tot}}$. The $N_{\mathrm{ch}}^{\mathrm{tot}}$ is determined using extrapolations of the measured data to the full extent in rapidity, and it also follows the trend for heavy-ion collisions.

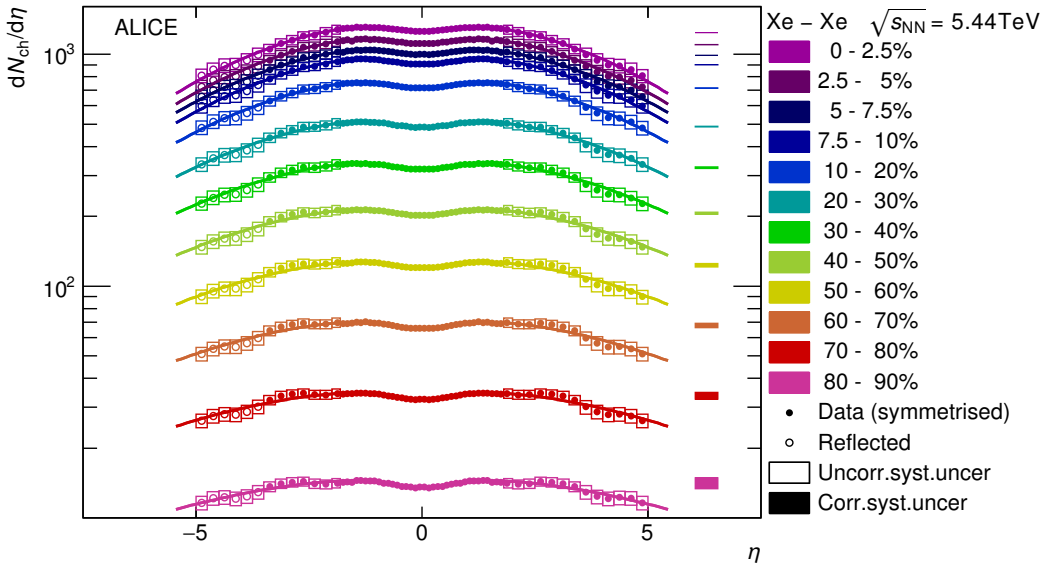

Figure 3.4: Charged-particle pseudorapidity density for 12 centrality classes over a broad η range in xenon–xenon collisions at $\sqrt{s_{\mathrm{NN}}} = 5.44$ TeV. Boxes around the points reflect the total systematic uncertainties, while the filled squares on the right reflect the normalization uncertainty from the centrality determination. Statistical errors are negligible. The reflection (open circles) of the $3.5 < \eta < 5$ values around $\eta = 0$ is also shown. The lines correspond to fits to a Gaussian distribution in rapidity y multiplied by an effective Jacobian of transformation from η to y. Taken from Ref. [4].

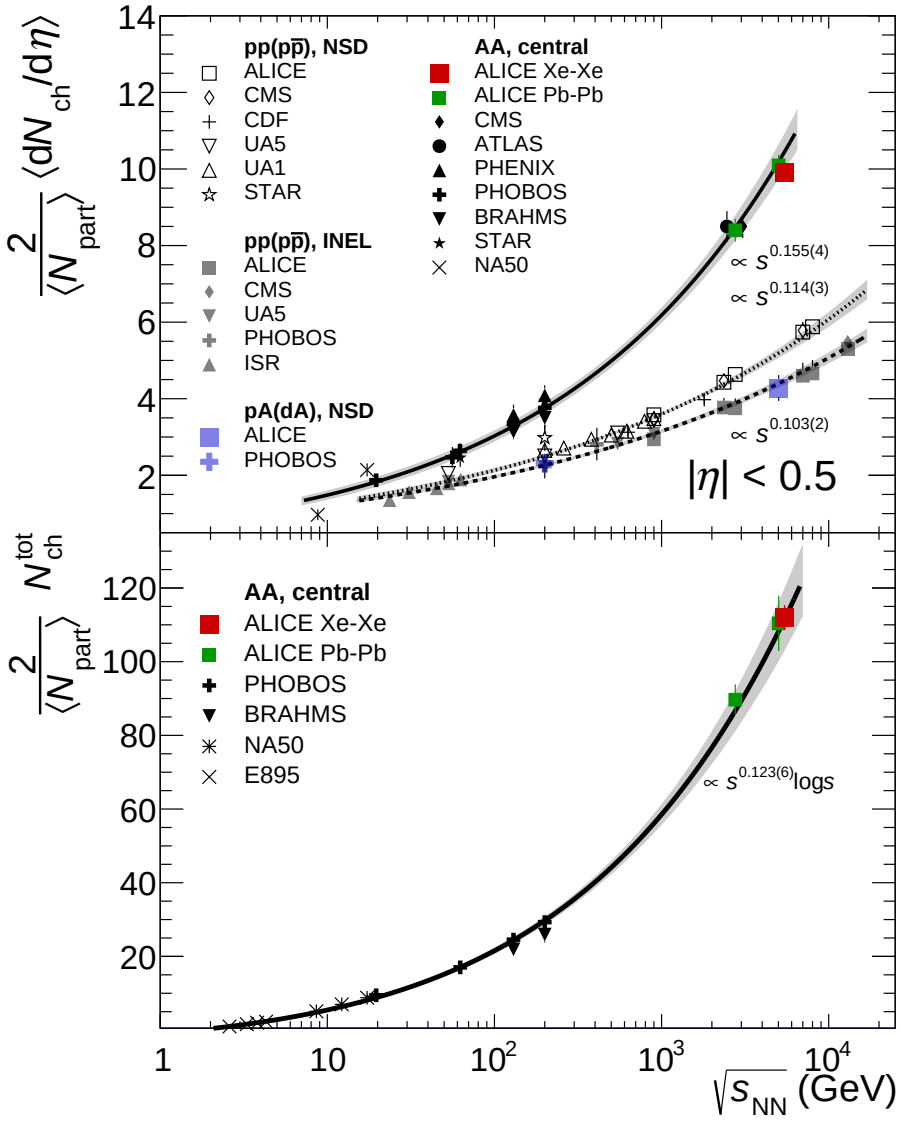

Figure 3.5: Values of $\frac{2}{\langle N_{\mathrm{part}} \rangle} \langle \mathrm{d}N_{\mathrm{ch}}/\mathrm{d}\eta \rangle$ (top) and $\frac{2}{\langle N_{\mathrm{part}} \rangle} N_{\mathrm{ch}}^{\mathrm{tot}}$ (bottom) for the 5% most central xenon–xenon collisions compared to previous measurements in lead–lead and gold–gold collisions as a function of $\sqrt{s_{\mathrm{NN}}}$ as well as for inelastic proton–proton, proton–antiproton and non-single-diffractive proton–nucleus and deuteron–nucleus collisions. The lines are power-law fits of the data, excluding xenon–xenon results. The central lead–lead measurements from CMS and ATLAS at 2.76 TeV have been shifted horizontally for clarity. Taken from Ref. [4].

The same variables are plotted against $\langle N_{\mathrm{part}} \rangle$ in Fig. 3.6, and they are compared to previous lead–lead ALICE measurements, and gold–gold and copper–copper RHIC measurements. $\frac{2}{\langle N_{\mathrm{part}} \rangle} \langle \mathrm{d}N_{\mathrm{ch}}/\mathrm{d}\eta \rangle$ and $\frac{2}{\langle N_{\mathrm{part}} \rangle} N_{\mathrm{ch}}^{\mathrm{tot}}$ increase from the most peripheral to the most central collisions by a factor of 2. The most peripheral collisions correspond to proton–proton and proton–nucleus collisions. A steeper increase, which might be caused by multiplicity fluctuations in the tail of the V0 amplitude distribution, is visible in the new xenon–xenon data. A negative binomial distribution Glauber fit reproduces this data accurately.

A different scaling is shown in Fig. 3.7, where the same variables are plotted as a function of $(\langle N_{\mathrm{part}} \rangle - 2)/(2A)$, where A is the atomic mass number. In this graph, all data follow a similar evolution with no steeper rise in the xenon–xenon data, which suggests, that the multiplicity of an event depends more on the collision's geometric properties than on the collision system size.

Figure 3.8 and Fig. 3.9 show the comparison to existing models of multiplicity dependent on the number of participants $\langle N_{\mathrm{part}} \rangle$ and pseudorapidity η, respectively.

In Fig. 3.8, the HIJING model is calibrated the same way as in Sec. 3.1 and again fails to describe the data. Implementing a hydrodynamical evolution of an initial state obtained with the HIJING AMPT model gives a better result than HIJING alone as it fits both shape and magnitude.

PYTHIA/Angantyr is an extension of the nucleon–nucleon collision model to heavy-ion collisions, which describes the data reasonably well.

EPOS LHC implements the separation of the initial state into a core and a corona. The corona contains participant nucleons that scatter only once, and the core those that scatter multiple times. However, this model underestimates the xenon–xenon data as it did underestimate the lead–lead data in Sec. 3.1.

Saturation-inspired models, such as rcBK-MC from Sec. 2.1, provide a good description of both the shape and the magnitude of the evolution, and the same applies to the EKRT model.

The CGC model from Sec. 2.2 is here denoted KLN and underestimates all measured data.

The pseudorapidity dependence of $\mathrm{d}N_{\mathrm{ch}}/\mathrm{d}\eta$, shown in Fig. 3.9, is overestimated at forward rapidity by the HIJING, AMPT, and PYTHIA/Angantyr models. However, the HIJING model describes xenon–xenon data better than the lead–lead data in Sec. 3.1. The EPOS LHC model underestimates the magnitude of multiplicity. The rcBK-MC does not cover the whole pseudorapidity range as it can be used only for rapidities far from the fragmentation region, and in the used range, it shows a narrower distribution than the measured data.

3.2.3 Summary

The xenon–xenon measurements done with ALICE discussed in this section correspond with previous heavy-ion measurements done with ALICE and RHIC. The

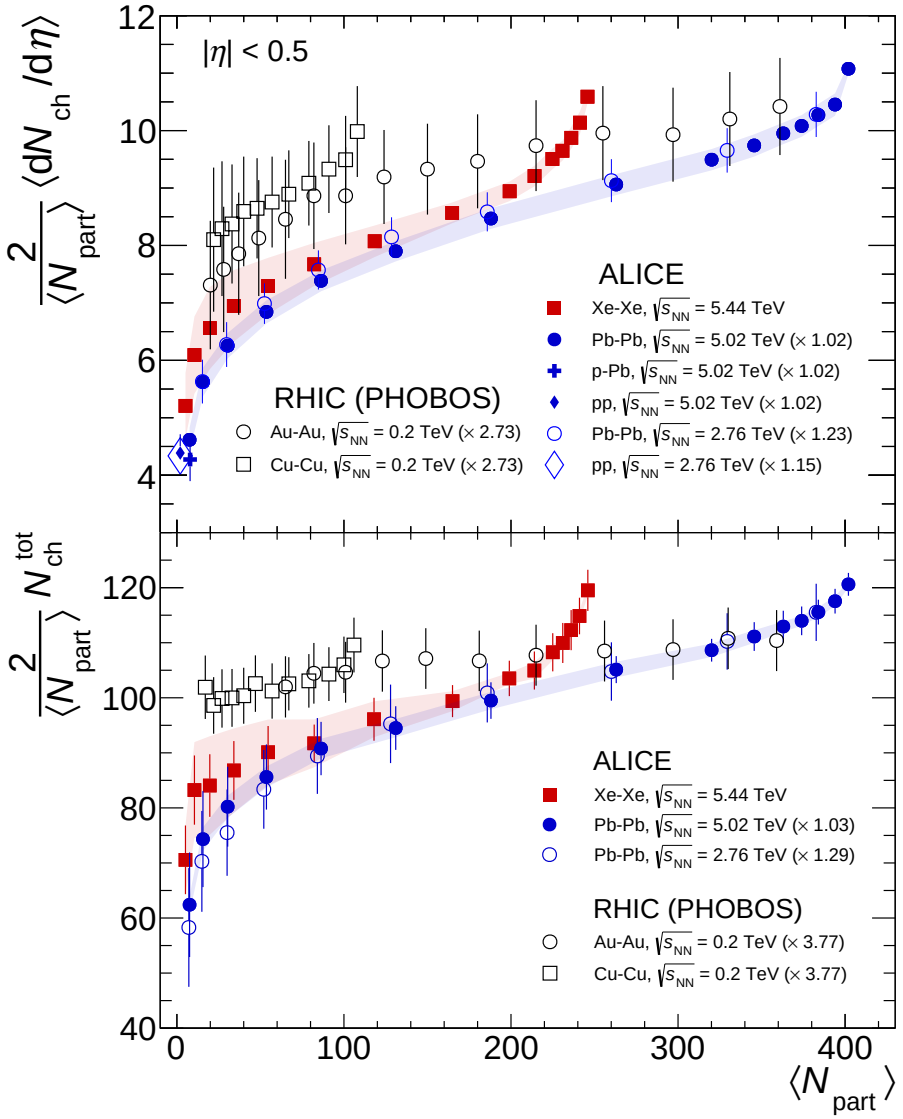

Figure 3.6: The $\frac{2}{\langle N_{\rm part}\rangle}\langle {\rm d}N_{\rm ch}/{\rm d}\eta\rangle$ (top) and $\frac{2}{\langle N_{\rm part}\rangle}N_{\rm ch}^{\rm tot}$ (bottom) for xenon–xenon collisions at $\sqrt{s_{\rm NN}} = 5.44$ TeV as a function of $N_{\rm part}$. The error bars indicate the point-to-point centrality-dependent uncertainties, whereas the shaded band shows the correlated contributions. Also shown in the figure is the result from inelastic proton–proton at $\sqrt{s} = 5.02$ TeV as well as non-single-diffractive proton–lead collisions and lead–lead collisions at $\sqrt{s_{\rm NN}} = 5.02$ TeV. The lead–lead data at $\sqrt{s_{\rm NN}} = 5.02$ TeV were re-analyzed in narrower centrality classes. Data from lower energies at $\sqrt{s_{\rm NN}} = 2.76$ TeV and 200 GeV are shown for comparison. Taken from Ref. [4].

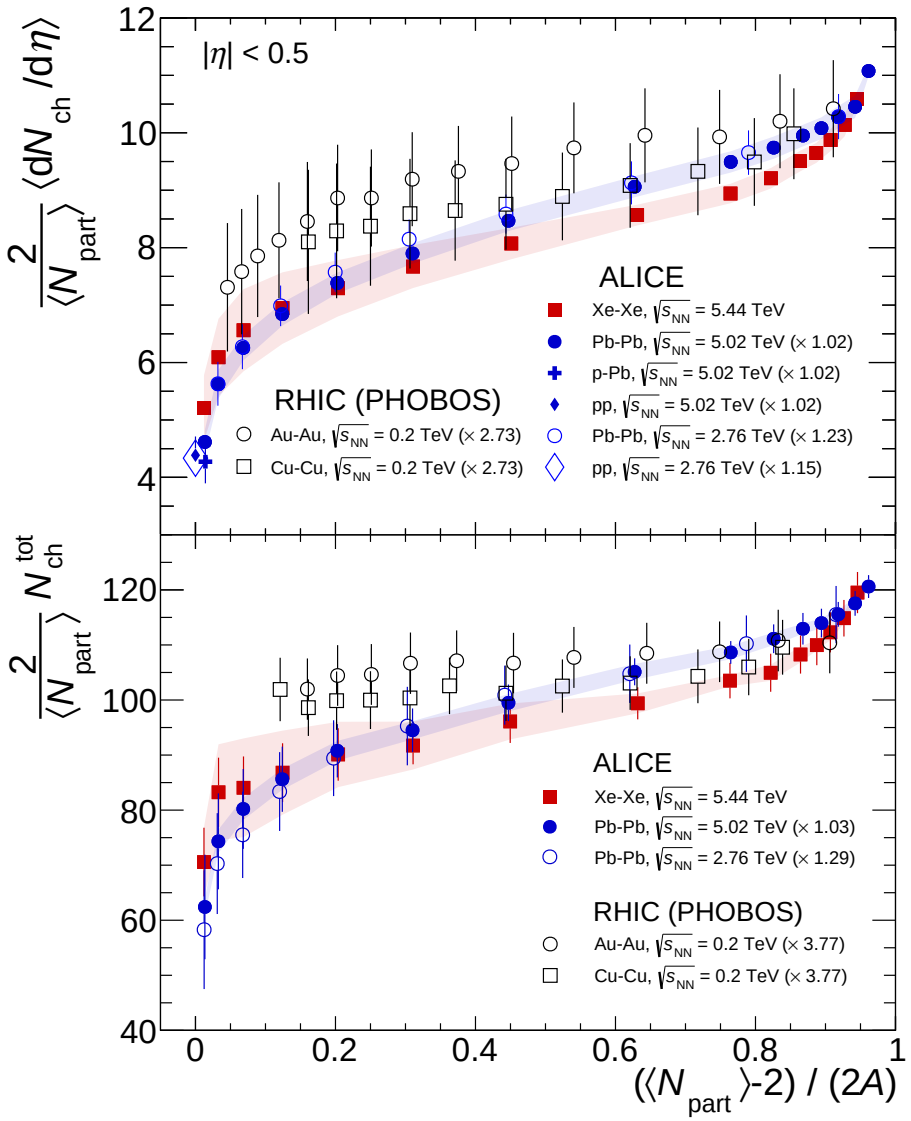

Figure 3.7: The $\frac{2}{\langle N_{\mathrm{part}}\rangle}\langle \mathrm{d}N_{\mathrm{ch}}/\mathrm{d}\eta\rangle$ (top) and $\frac{2}{\langle N_{\mathrm{part}}\rangle}N_{\mathrm{ch}}^{\mathrm{tot}}$ (bottom) for xenon–xenon collisions at $\sqrt{s_{\mathrm{NN}}} = 5.44$ TeV as a function of $(\langle N_{\mathrm{part}}\rangle - 2)/(2A)$. Taken from Ref. [4].

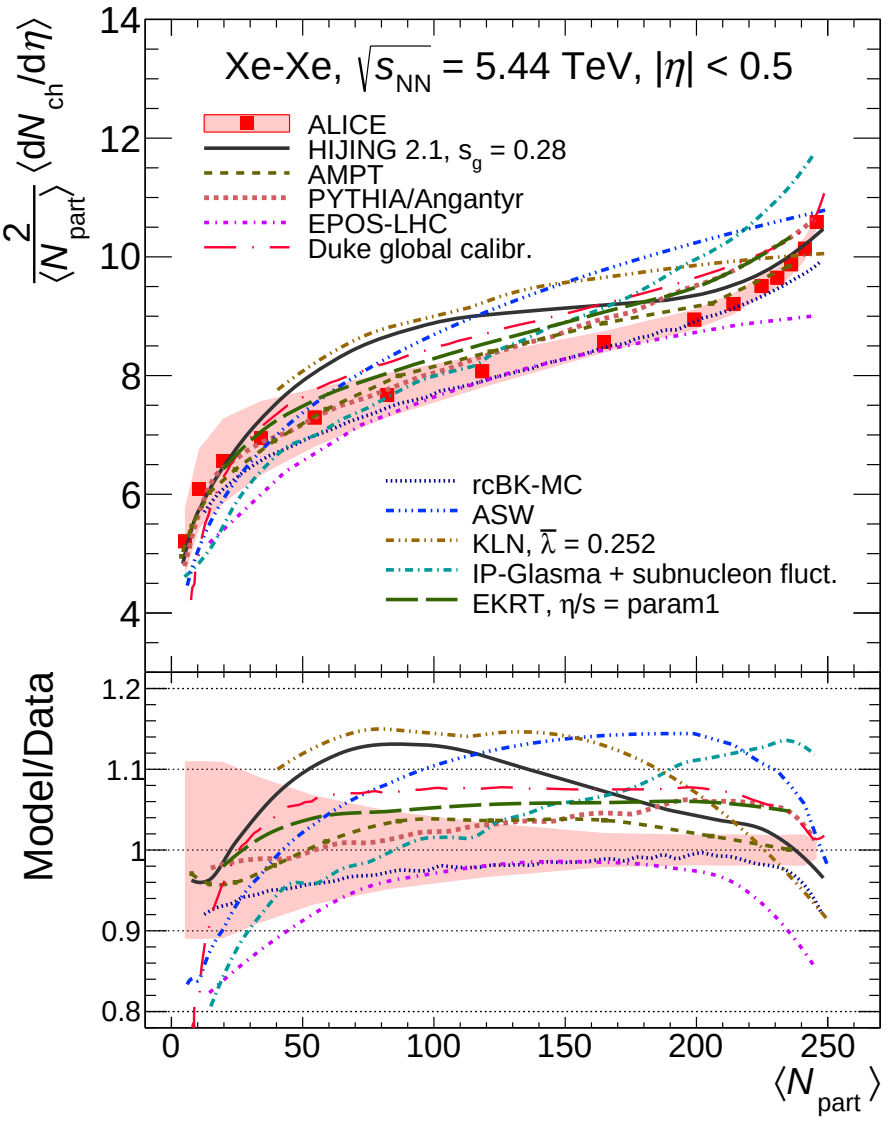

Figure 3.8: The $\frac{2}{\langle N_{\mathrm{part}} \rangle} \langle \mathrm{d}N_{\mathrm{ch}}/\mathrm{d}\eta \rangle$ for xenon–xenon collisions at $\sqrt{s_{\mathrm{NN}}} = 5.44$ TeV as a function of $\langle N_{\mathrm{part}} \rangle$ compared to model predictions. The bottom panel shows the ratio of the models to the data. The shaded band around the points reflects the correlated systematic uncertainties. Taken from Ref. [4].

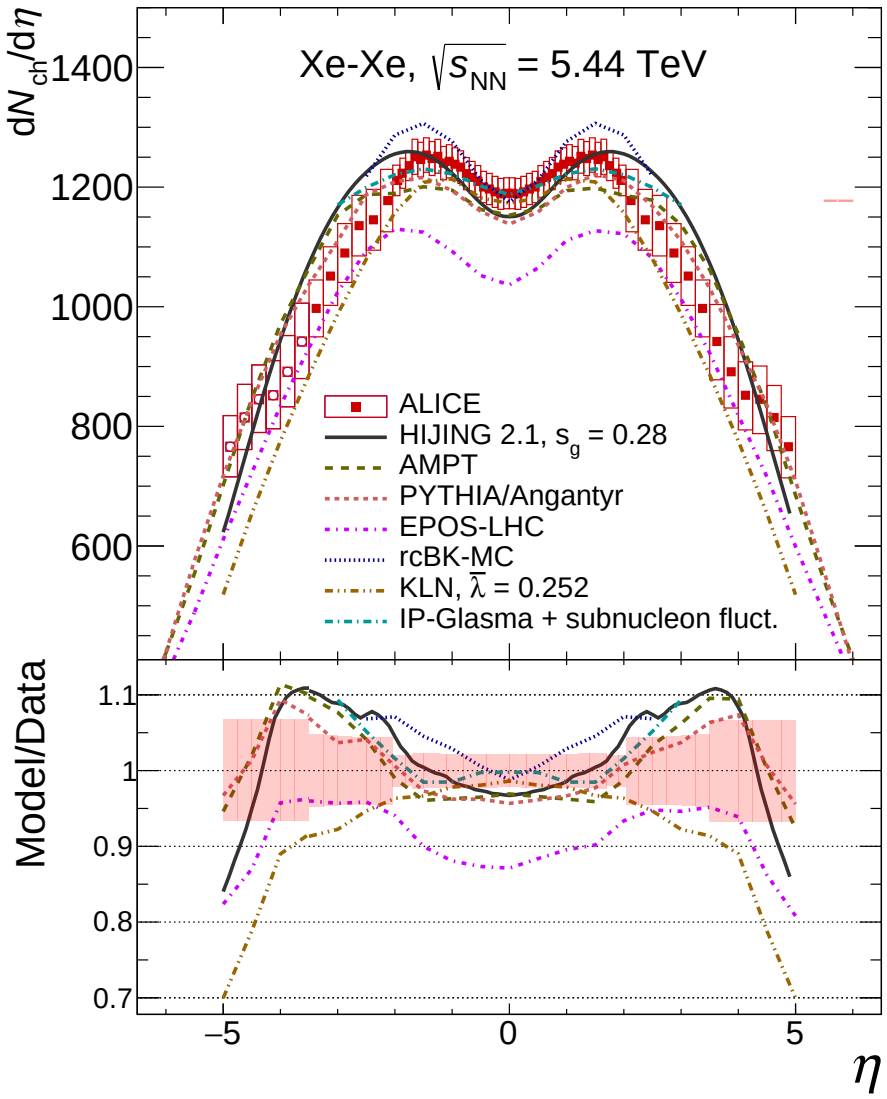

Figure 3.9: Comparison of $\mathrm{d}N_{\mathrm{ch}}/\mathrm{d}\eta$ as a function of η in the 0–5% central class to model predictions. The bottom panel shows the ratio of the models to the data. Boxes around the points reflect the total uncorrelated systematic uncertainties. Taken from Ref. [4].

multiplicity scaled per participant pairs $\frac{2}{\langle N_{\mathrm{part}} \rangle} \langle \mathrm{d}N_{\mathrm{ch}}/\mathrm{d}\eta \rangle$ follows the same power-law dependence on energy as was described in previous section Sec. 3.1.

From the difference between Fig. 3.6 and Fig. 3.7 that show the dependence of the multiplicity scaled per participant pairs $\frac{2}{\langle N_{\mathrm{part}} \rangle} \langle \mathrm{d}N_{\mathrm{ch}}/\mathrm{d}\eta \rangle$ on $\langle N_{\mathrm{part}} \rangle$ and $(\langle N_{\mathrm{part}} \rangle - 2)/(2A)$, respectively, indicates that there exists a stronger dependence on the collision geometry than on the size of colliding systems.

Models describe the xenon–xenon data with similar precision as the lead–lead data from Sec. 3.1. Only the HIJING model gives a better prediction for the xenon–xenon collisions, than for the lead–lead.

Chapter 4

Analysis of Run 3 lead-lead collision data

The main focus of this chapter is a simple analysis of lead-lead data measured by the detector complex of ALICE on the 18th of November 2022 and of the corresponding simulations. The centre-of-mass energy was $\sqrt{s_{\mathrm{NN}}} = 5.36$ TeV. The analysis was carried out using the O^2 software and was run over data on the Grid using the ALICE system called Hyperloop. The script used for the analysis is a modification of the official tutorial script within the PWGMM group. However, the script used for calculating the pseudorapidity density was created solely by me.

The lead-lead runs used are 529397, 529399, 529414, and 529418 for pass5. The used Monte Carlo simulated data were unanchored because anchored data were not available during the creation of this thesis. Therefore, the resolutions of the measurements cannot be calculated. Anchored simulations use the same conditions dataset and the same number of generated events as the RAW data runs. I used runs 310015, 310016, and 310017 from LHC22i1 and 311010 and 311011 from LHC22k3b2.

As the tracking detector has a finite size, the efficiency of the measurements differs with position. The innermost layer of the ITS is approximately 27 cm wide in the longitudinal direction Ref. [15]. The particles closer to the middle of the detector are detected with higher efficiency than those further away from it. The detector efficiency is dependent on the multiplicity of a given collision and slightly on the pseudorapidity of the particle. The measured data need to be corrected for this.

The following formula has to be used to obtain the corrected pseudorapidity distributions.

$$\left.\frac{1}{N_{evt}}\frac{dN}{d\eta}\right|_{\eta=\eta'} \sim \frac{\int_{z_{min}}^{z_{max}(\eta')}(\eta')N^{*}_{\mathrm{trk}}(Z_{\mathrm{vtx}},\eta')/\epsilon_{\mathrm{trk}}(Z_{\mathrm{vtx}},\eta')}{\int_{z_{min}}^{z_{max}(\eta')}(\eta')\sum_{N}N^{*}_{\mathrm{evt}}(Z_{\mathrm{vtx}},N)/\epsilon_{\mathrm{evt}}(Z_{\mathrm{vtx}},N)}, \tag{4.1}$$

where N is the number of particles (multiplicity), N_{trk} is the number of tracks, N_{evt} is the number of events, Z_{vtx} is the position of the vertex on the z axis, and η is the pseudorapidity. Starred quantities are from the real data, and ϵ marks the

efficiencies determined from simulations using the following formulas

$$\epsilon_{\mathrm{trk}}(Z_{\mathrm{vtx}}, \eta) = \frac{N_{\mathrm{trk}}^{\mathrm{rec}}(Z_{\mathrm{vtx}}, \eta)}{N_{\mathrm{trk}}^{\mathrm{gen}}(Z_{\mathrm{vtx}}, \eta)}, \tag{4.2}$$

$$\epsilon_{\mathrm{evt}}(Z_{\mathrm{vtx}}, \eta) = \frac{N_{\mathrm{evt}}^{\mathrm{rec}}(Z_{\mathrm{vtx}}, N)}{N_{\mathrm{evt}}^{\mathrm{gen}}(Z_{\mathrm{vtx}}, N)}. \tag{4.3}$$

This chapter has the following structure. The event selections used are listed in Sec. 4.1. Nextly, Sec. 4.2 is dedicated to the primary vertex reconstruction, Sec. 4.3 to distance of the closest approach measurements and distribution of tracks in pseudorapidity η and in azimuthal angle Φ, and Sec. 4.4 focuses on momentum distributions. The multiplicity and the pseudorapidity density are studied in Sec. 4.5. Corrections and further event selections still need to be added.

4.1 Analysis selections

The first step in an analysis is to reconstruct collisions, or more precisely, primary vertices, with all the corresponding tracks found in the central barrel of ALICE. The following cuts are then applied to this data.

Two selection criteria were applied in this analysis. The limit on the distance of the closest approach in xy plane DCAxy was 0.2 cm. Badly tracked particles were excluded using a '`track.tpcNClsCrossedRows() < 70`' criterion.

LHC22i1 MC simulated data with these selection criteria produced 2.50×10^7 events, and LHC22k3b2 MC simulated data produced 1.59×10^5 events. Measured data LHC22s counted for pass5 1.29×10^6 events.

4.2 Vertex reconstruction

The distribution of the z position of the primary vertices is for MC simulated data LHC22i1, LHC22k3b2, and for the LHC22s measured data from pass5 in Fig. 4.1. Both the MC simulated data and the measured ones follow the expected normal distribution. However, the measured data have a shifted mean from the MC simulations, and the width of the distributions also differ.

The z position distribution of the primary vertex and the corresponding number of tracks $\mathrm{N_{trk}}$ is shown in Fig. 4.2 for LHC22i1, LHC22k3b2, and LHC22s-pass5, respectively.

The track's pseudorapidity and assigned z vertex position are shown in Fig. 4.3 for LHC22i1, LHC22k3b2, and LHC22s-pass5, respectively.

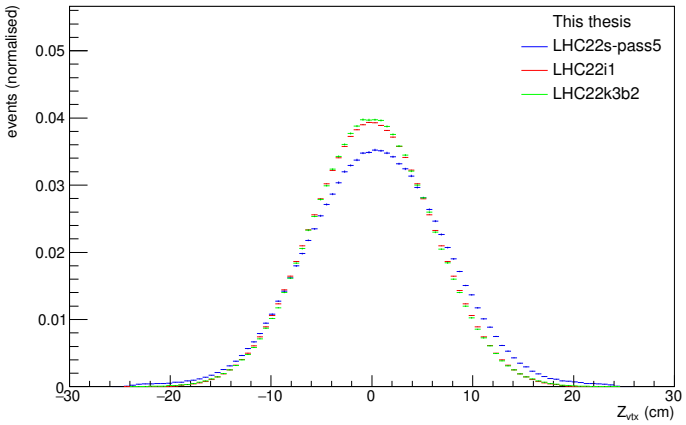

Figure 4.1: The distribution of z position of the primary vertex.

4.3 Spatial distribution

In this section, the results for the tracks pseudorapidity distribution, distance of the closest approach in xy plane and along the z axis, and the track distribution in pseudorapidity η and in azimuthal angle Φ are shown for MC simulated data LHC22i1 and LHC22k3b2, and LHC22s measured data from pass5.

There is an evident difference between the measured data and the MC simulations LHC22i1 in the tracks pseudorapidity distribution shown in Fig. 4.4. However, the difference between the measured data and MC simulations LHC22k3b2 is negligible. Although, neither set of simulated data is anchored in the measurements.

The DCA distributions, shown in Fig. 4.5 and Fig. 4.6, are visibly narrower for the MC simulated data.

The $\Phi - \eta$ distribution of the measured data has a slight gap around π in Φ, which is not present in the simulations. This gap might have been caused by a detector's inefficiency.

4.4 Momentum distributions

This section contains the plots for the transverse momentum distributions of the MC simulated data LHC22i1 and LHC22k3b2 and LHC22s measured data from pass5.

As can be seen in Fig. 4.8, the transverse momentum distributions are similar for measured and simulated data. However, there is a steeper decrease of higher p_t particles in the measured data compared to the simulated ones.

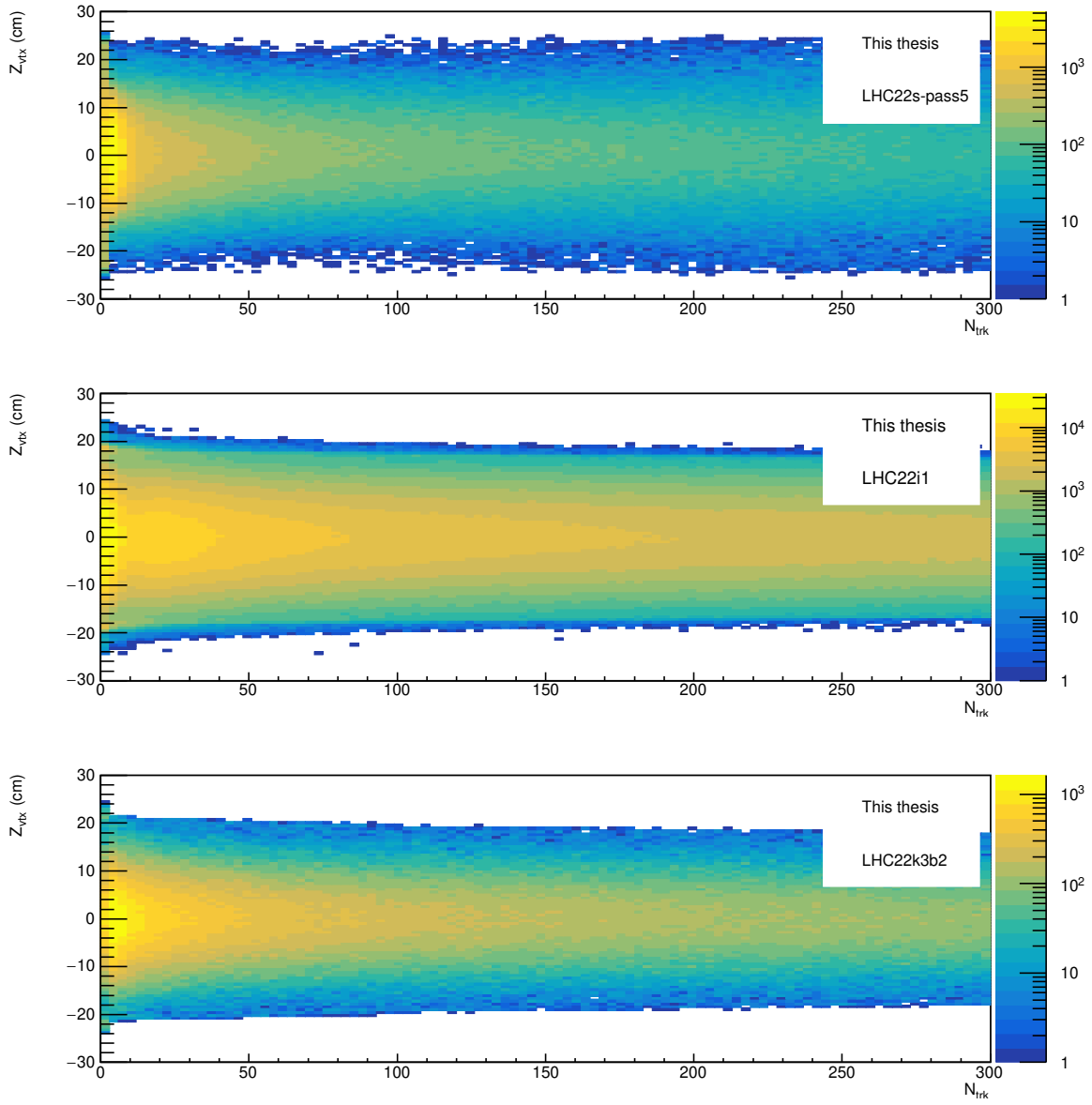

Figure 4.2: The z position distribution of the primary vertex and the corresponding number of tracks N_{trk}.

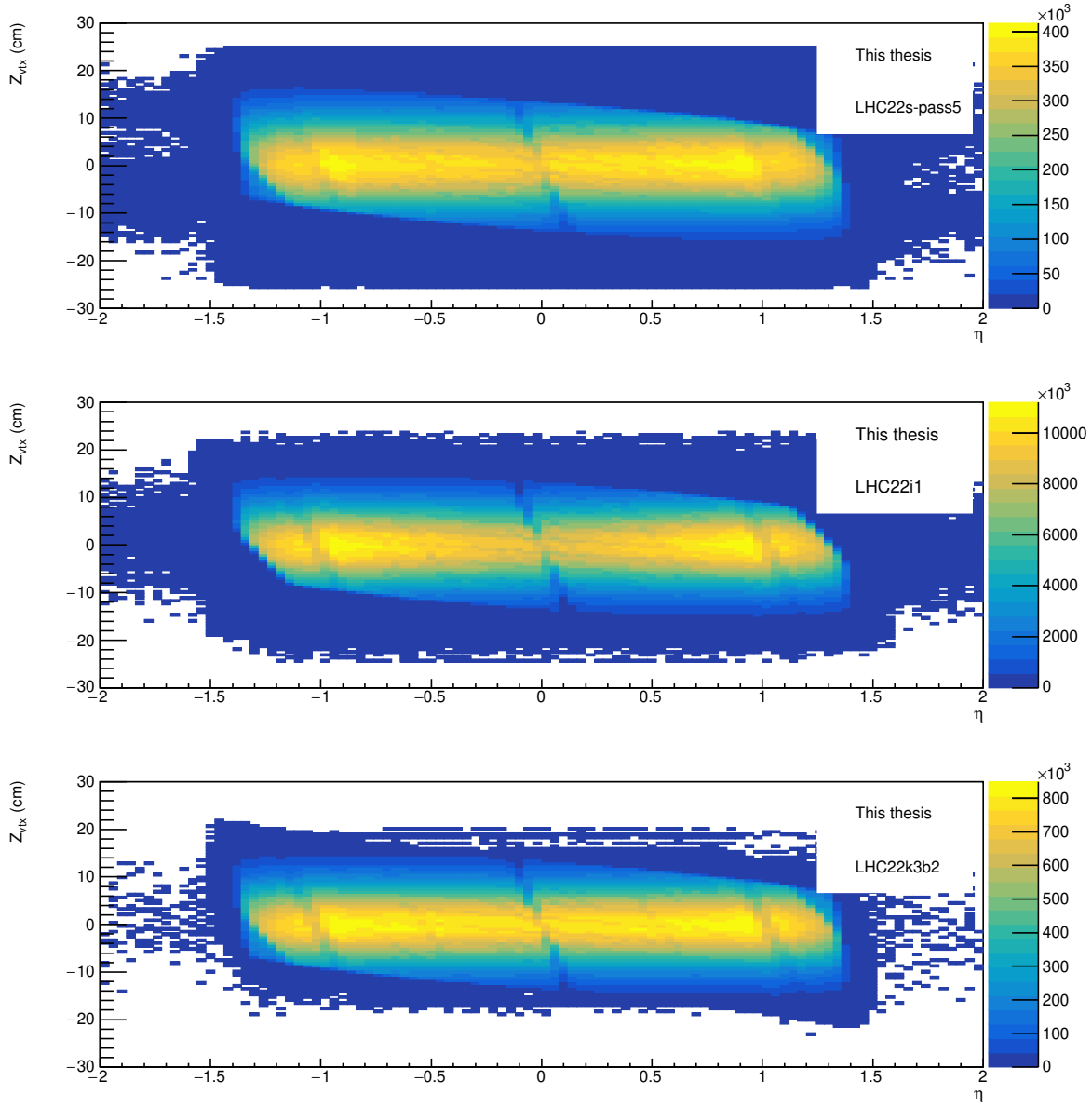

Figure 4.3: The pseudorapidity η and z position distribution of the primary vertex.

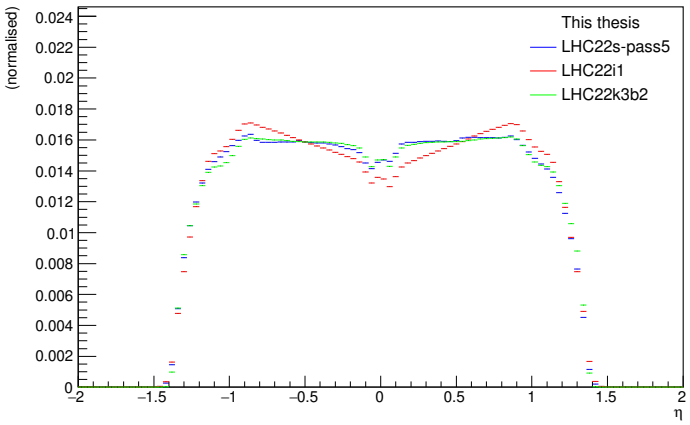

Figure 4.4: The tracks pseudorapidity distributions.

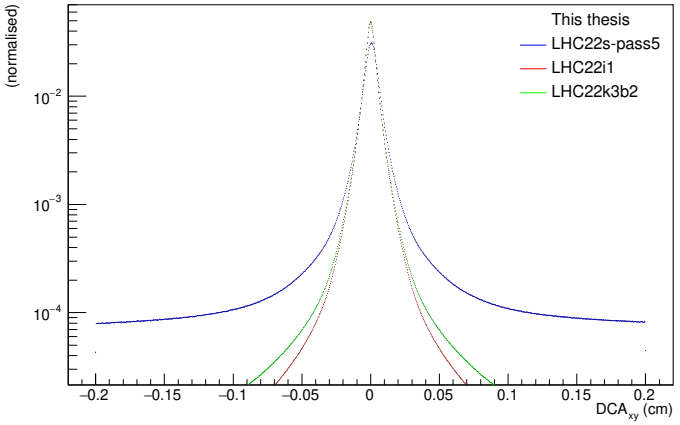

Figure 4.5: The distances of the closest approach in xy plane DCAxy.

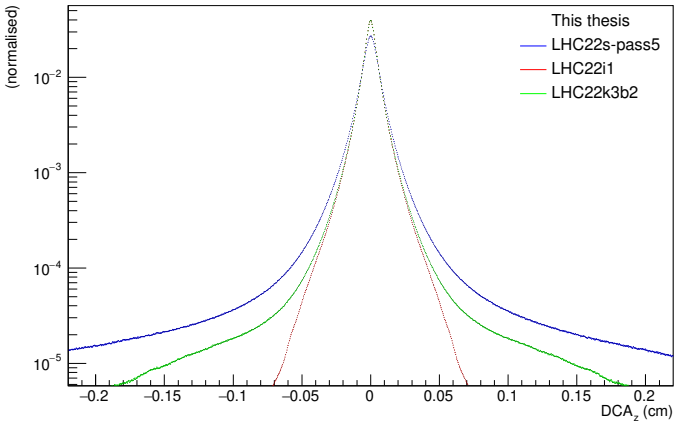

Figure 4.6: The distances of the closest approach in z DCAz.

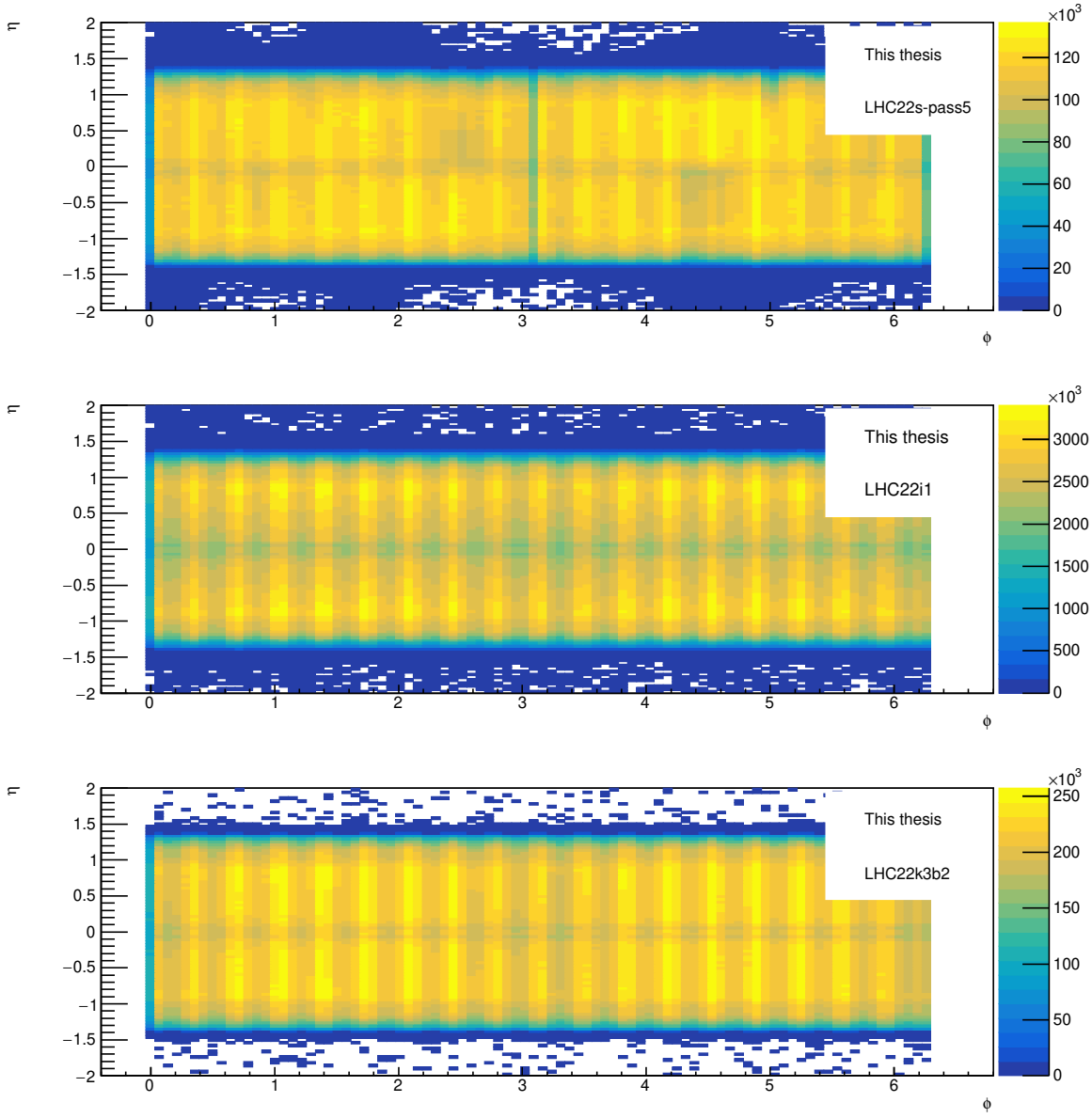

Figure 4.7: The tracks distributions in pseudorapidity η and azimuthal angle Φ.

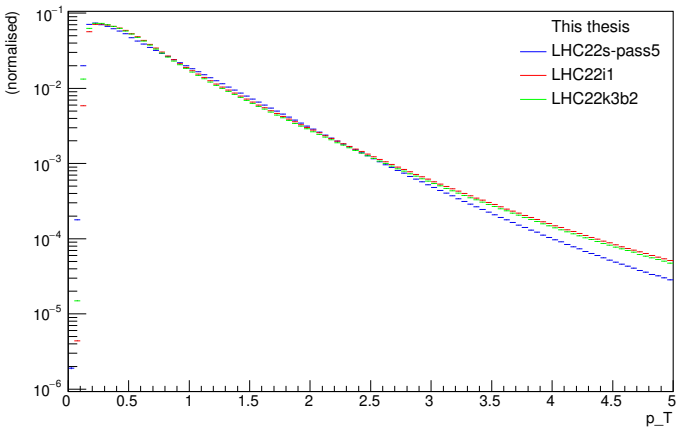

Figure 4.8: Transverse momentum distributions.

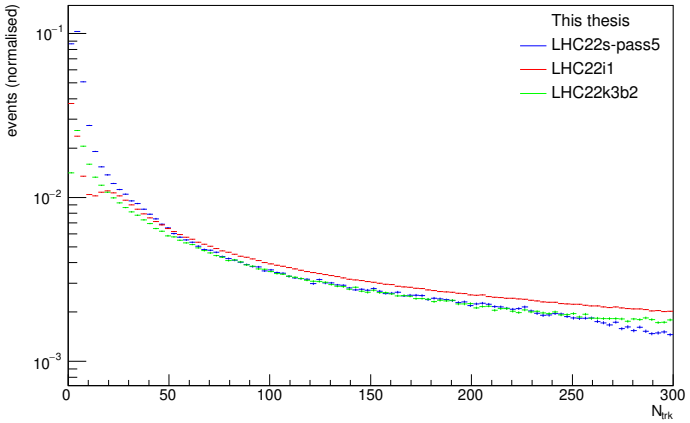

Figure 4.9: Charged particle multiplicity distributions.

4.5 Multiplicity

Plots of multiplicity distributions for MC simulated data LHC22i1 and LHC22k3b2 and LHC22s measured data from pass5 are in Fig. 4.9. There is a higher number of low-multiplicity events and a steeper decrease in the number of collisions with higher multiplicity present in the real data. The MC simulations LHC22i1 have an unexplained peak around 25.

The pseudorapidity density distribution is shown in Fig. 4.1. The corrections from Eq. 4.3 and Eq. 4.2 are not yet applied. However, the pseudorapidity density has the expected distribution.

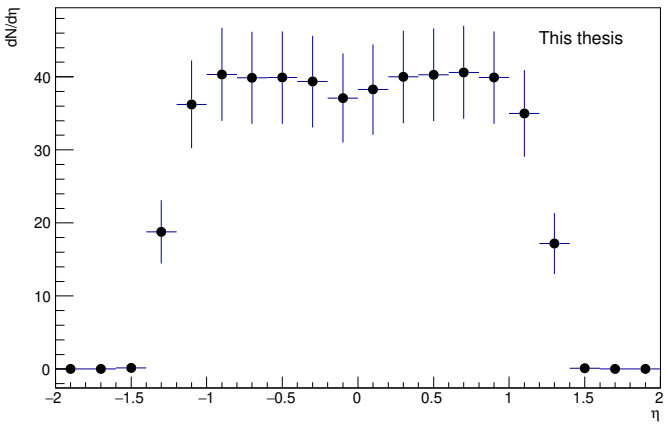

Figure 4.10: The pseudorapidity density distribution without efficiency corrections.

Summary

This report begins with a description of the ALICE detector complex during Run 2 and its upgrade for Run 3. The first chapter ends with a summary of the workings of the new Online-Offline analysis software O^2. The second chapter focuses on the Color Glass Condensate model and two different approaches for particle production calculation based on this model. The published measurements of Run 2 ALICE data from lead–lead and xenon–xenon collisions are summarised in Chapter 3.

The final chapter is an overview of my analysis of Monte Carlo simulated data LHC22i1 and LHC22k3b2 and of the data measured during the LHC22s period on the 18th of November 2022 with the center-of-mass energy of $\sqrt{s} = 5.36$ TeV. The whole analysis was carried out using the O^2 software and was run over data on the Grid using the ALICE system called Hyperloop. The results shown in this thesis are preliminary, and more advanced analysis is needed. For example, the corrections for efficiency varying with the z position of the primary vertex need to be added. The MC simulated data are consistent with the measured data.

The upgraded ALICE detector complex with the new analysis software will allow more precise and faster analysis of heavy-ion collisions. This report aimed to produce a simple first analysis of the latest data, which was successfully achieved. These results and the knowledge gained from this analysis will be the basis of my further research.

Bibliography

[1] Javier L. Albacete and Adrian Dumitru. "A model for gluon production in heavy-ion collisions at the LHC with rcBK unintegrated gluon densities". In: (2011). arXiv: 1011.5161 [hep-ph].

[2] Dmitri Kharzeev, Eugene Levin, and Marzia Nardi. "Color glass condensate at the LHC: hadron multiplicities in *pp*, *pA* and *AA* collisions". In: *Nuclear Physics A* 747.2-4 (Jan. 2005), pp. 609–629. DOI: 10.1016/j.nuclphysa.2004.10.018. URL: https://doi.org/10.1016%2Fj.nuclphysa.2004.10.018.

[3] ALICE Collaboration. "Centrality Dependence of the Charged-Particle Multiplicity Density at Midrapidity in Pb-Pb Collisions at $\sqrt{s_{NN}} = 5.02$ TeV". In: *Physical Review Letters* 116.22 (June 2016). DOI: 10.1103/physrevlett.116.222302. URL: https://doi.org/10.1103%2Fphysrevlett.116.222302.

[4] ALICE Collaboration. "Centrality and pseudorapidity dependence of the charged-particle multiplicity density in Xe-Xe collisions at $\sqrt{s_{NN}} = 5.44$ TeV". In: *Physics Letters B* 790 (Mar. 2019), pp. 35–48. DOI: 10.1016/j.physletb.2018.12.048. URL: https://doi.org/10.1016%2Fj.physletb.2018.12.048.

[5] *LHC Pb collisions*. 2023. URL: https://www.lhc-closer.es/taking_a_closer_look_at_lhc/0.lhc_pb_collisions.

[6] *LHC commissioning*. 2023. URL: http://lhc-commissioning.web.cern.ch/schedule/LHC-long-term.htm.

[7] Hesounova Helena. "Multiplicity measurements in pp collisions with ALICE during the LHC Run 3 [Bachelor thesis, Czech Technical University]". 2022. URL: http://hdl.handle.net/10467/104080.

[8] *A Large Ion Collider Experiment*. 2022. URL: https://alice-collaboration.web.cern.ch/.

[9] *ALICE Physics and Detectors*. 2022. URL: https://alice.cern/node/5511.

[10] Arturo Tauro. "ALICE Schematics". General Photo. May 2017. URL: https://cds.cern.ch/record/2263642.

[11] ALICE Collaboration. "ALICE upgrades during the LHC Long Shutdown 2". In: (2023). eprint: 2302.01238. URL: https://arxiv.org/abs/2302.01238.

[12] F. Reidt. "Upgrade of the ALICE ITS detector". In: *Nuclear Instruments and Methods in Physics Research Section A: Accelerators, Spectrometers, Detectors and Associated Equipment* 1032 (June 2022), p. 166632. DOI: 10.1016/j.nima.2022.166632. URL: https://doi.org/10.1016%2Fj.nima.2022.166632.

[13] Maciej Slupecki. "The Fast Interaction Trigger for the ALICE Upgrade [Dissertation, University of JYU]". In: (2020). URL: https://jyx.jyu.fi/handle/123456789/69664#.

[14] ALICE Collaboration. "Technical Design Report for the Upgrade of the Online-Offline Computing System". In: (2023). URL: https://indico.ifj.edu.pl/event/101/contributions/2/attachments/4/4/2015-Mar-05-paper_draft-O2_TDR_ALICE_comments.pdf.

[15] Felix Reidt. "Studies for the ALICE Inner Tracking System Upgrade [Doctoral thesis, Heidelberg University". In: (2016). Presented 28 Apr 2016. URL: https://cds.cern.ch/record/2151986.